CHAPTER IV
RESULTS AND DISCUSSION

4.1 Characterization Results of TiO_2 Photocatalysts

The physicochemical properties of the mesoporous-assembled TiO_2 nanoparticle synthesized by a sol-gel process with the aid of a structure-directing surfactant could be influenced by many factors, especially calcination temperature. In this study, the synthesized mesoporous-assembled TiO_2 calcined at various temperatures was investigated, as compared with various types of commercial TiO_2, namely P-25 TiO_2, ST-01 TiO_2, and JRC-03 TiO_2.

4.1.1 TG-DTA Analysis

The TG-DTA curves were used to study thermal decomposition behavior of the synthesized TiO_2 and to obtain its suitable calcination temperature, as shown in Figure 4.1. The DTA curve shows three main exothermic regions. The details of the position of the exothermic peaks, as well as their corresponding weight loss, are given in Table 4.1. The removal of physisorbed water molecules could contribute to the existence of the first small exothermic peak, with its position lower than 150°C. The second exothermic peak between 150-300°C, with its maximum at 262.5°C, is very sharp and narrow and is attributed to the burnout of the LAHC surfactant. The peaks in the third exothermic region between 300-500°C are weaker and corresponds to the crystallization process of the photocatalyst and also the removal of chemisorbed water molecules (Hague *et al.*, 1994). From the TG curve, the dominant weight loss of 26.82 wt.% was observed due to the removal of the surfactant photocatalyst structure. Since the TG curve shows that no significant weight loss was observed beyond 500°C with total weight loss of 39.52 wt.% up to this temperature, the calcination temperature at this value, i.e. 500°C, was sufficient for removal of the organic surfactant molecules, as well as the crystallization of TiO_2 photocatalyst.

Table 4.1 Thermal decomposition behavior of the synthesized TiO_2 photocatalyst from TG-DTA analysis

Photocatalyst	Position of exothermic peak (°C)				Corresponding weight loss (wt.%)				
	1st peak	2nd peak	3rd peak	4th peak	1st peak	2nd peak	3rd peak	4th peak	Total
Synthesized TiO_2	57.6	262.5	339.5	422.3	1.53	26.82	7.28	3.89	39.52

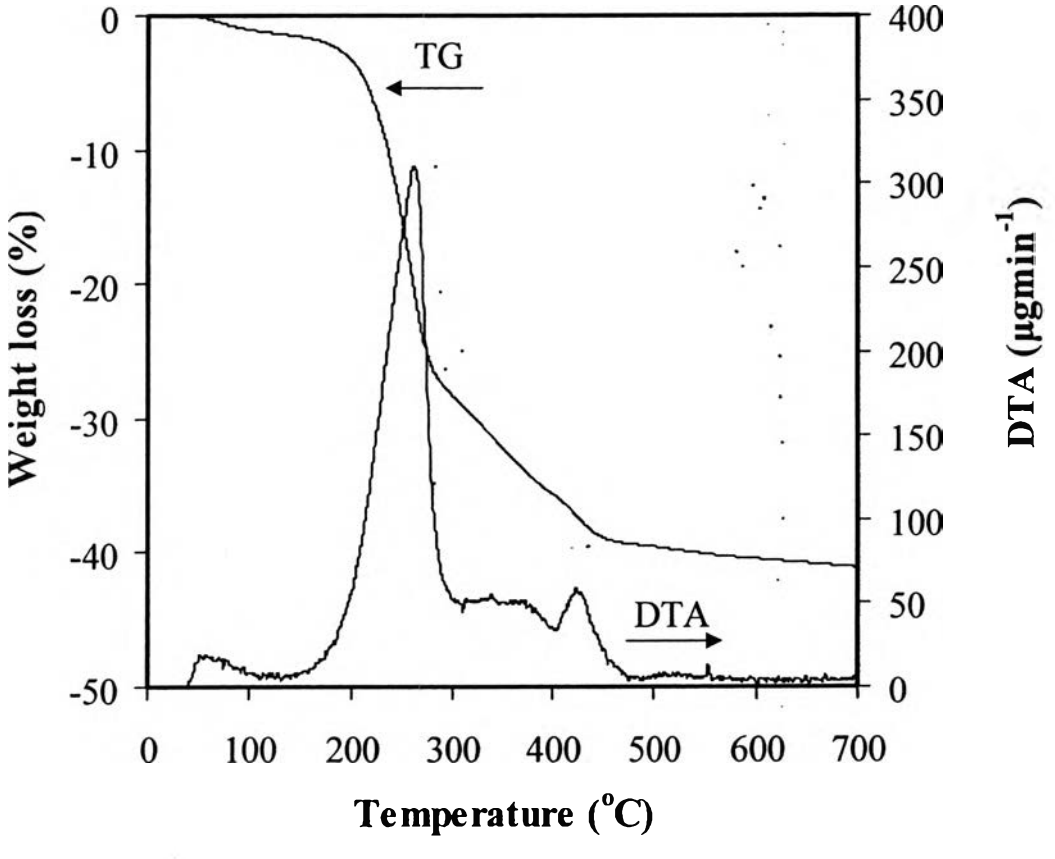

Figure 4.1 TG-DTA curves of the as-synthesized TiO_2 (dried sample).

4.1.2 N_2 Adsorption-Desorption Analysis

In order to verify the mesoporosity of the photocatalyst samples, N_2 adsorption-desorption analysis is very powerful technique normally used. The N_2 adsorption-desorption isotherms of the synthesized TiO_2 calcined at 500 and 600°C exhibited typical IUPAC type IV pattern (Rouquerol *et al.*, 1999), as shown in Figures 4.2 and 4.3, respectively. The hysteresis loop is ascribed to the existence of mesoporous structure (mesopore size between 2-50 nm) in the obtained products. A sharp increase in adsorption volume of N_2 was observed and located in the P/P_0 range of 0.5-0.9. This sharp increase can be assigned to the capillary condensation, indicating good homogeneity of the samples and fairly small pore size since the P/P_0 position of the inflection point is directly related to pore dimension. As illustrated in the inset of Figures 4.2 and 4.3, the pore size distribution obtained from this modified sol-gel process is quite narrow, implying good quality of the samples.

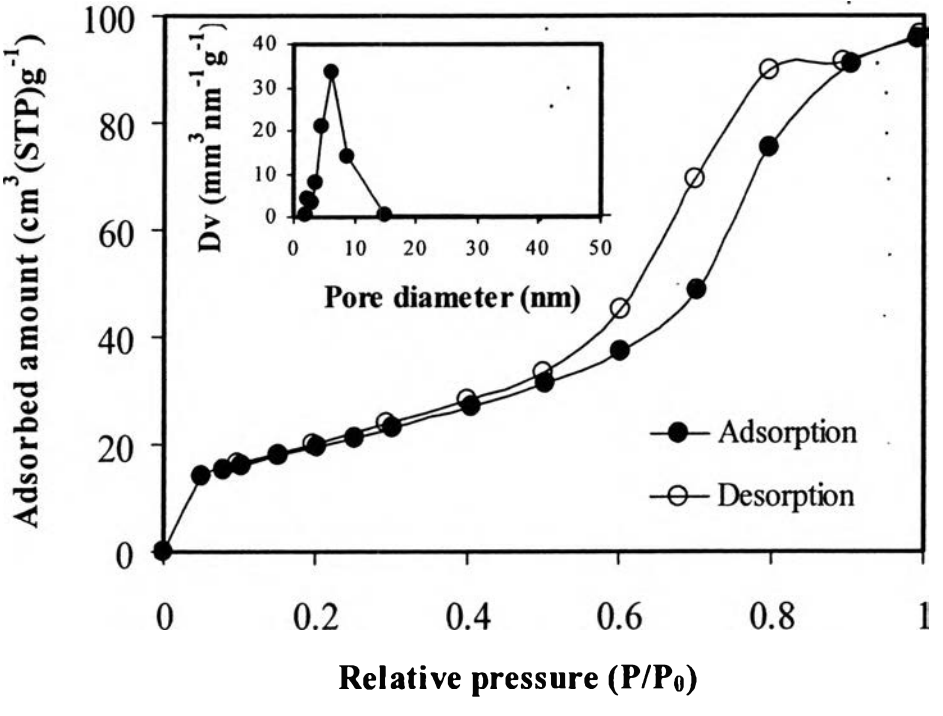

Figure 4.2 N_2 adsorption-desorption isotherms of the synthesized mesoporous-assembled TiO_2 calcined at 500°C for 4 h (Inset: Pore size distribution).

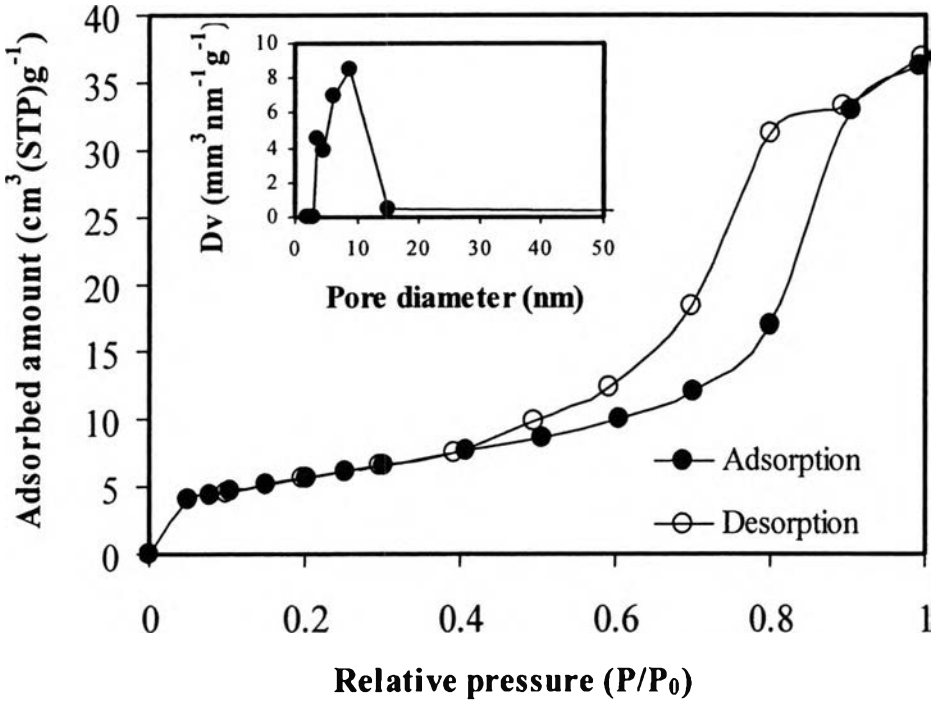

Figure 4.3 N_2 adsorption-desorption isotherms of the synthesized mesoporous-assembled TiO_2 calcined at 600°C for 4 h (Inset: Pore size distribution).

For the commercial P-25 TiO_2, ST-01 TiO_2, and JRC-03 TiO_2, N_2 adsorption-desorption isotherms correspond to IUPAC type II pattern (Rouquerol *et al.*, 1999), as depicted in Figures 4.4, 4.5, and 4.6, respectively. It is apparent that all commercial TiO_2 photocatalysts exhibited non-mesoporous characteristic due to the absence of dominant hysteresis loop and adsorption plateau at high relative pressure. No capillary condensation of N_2 into the pore was observed since the desorption isotherm was insignificantly different from the adsorption one. The pore size distribution of all commercial TiO_2 photocatalysts, as shown in the inset of Figures 4.4, 4.5, and 4.6, is quite broad. These results show that the pore sizes of commercial TiO_2 are quite large in average since their pore size distributions not only exist in the mesopore region (mesopore size between 2-50 nm) but also mostly cover the macropore region (macropore size > 50 nm).

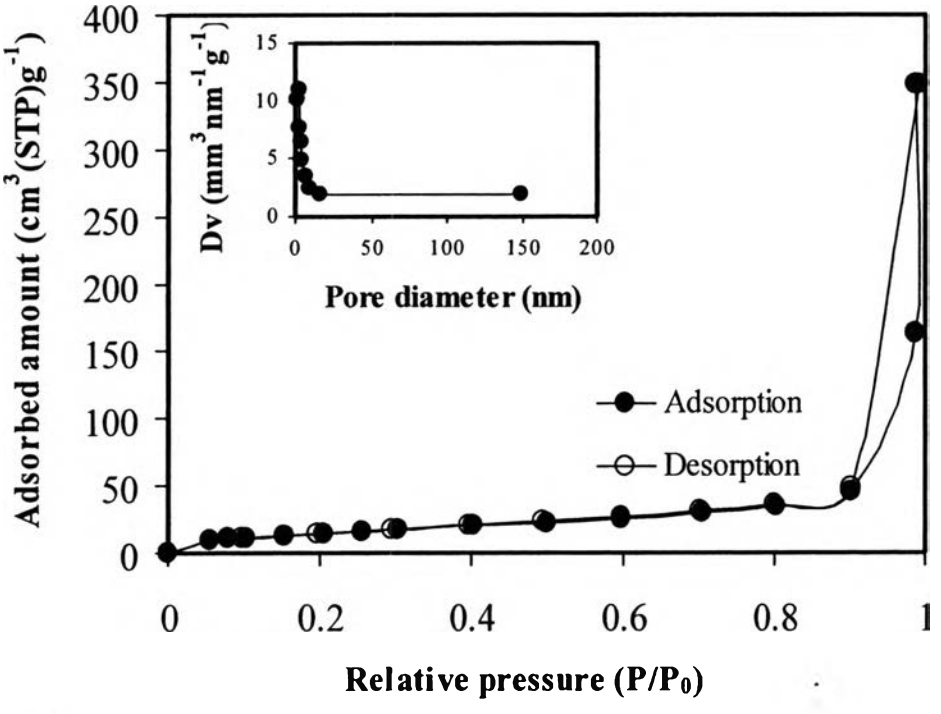

Figure 4.4 N_2 adsorption-desorption isotherms of the commercial P-25 TiO_2 (Inset: Pore size distribution).

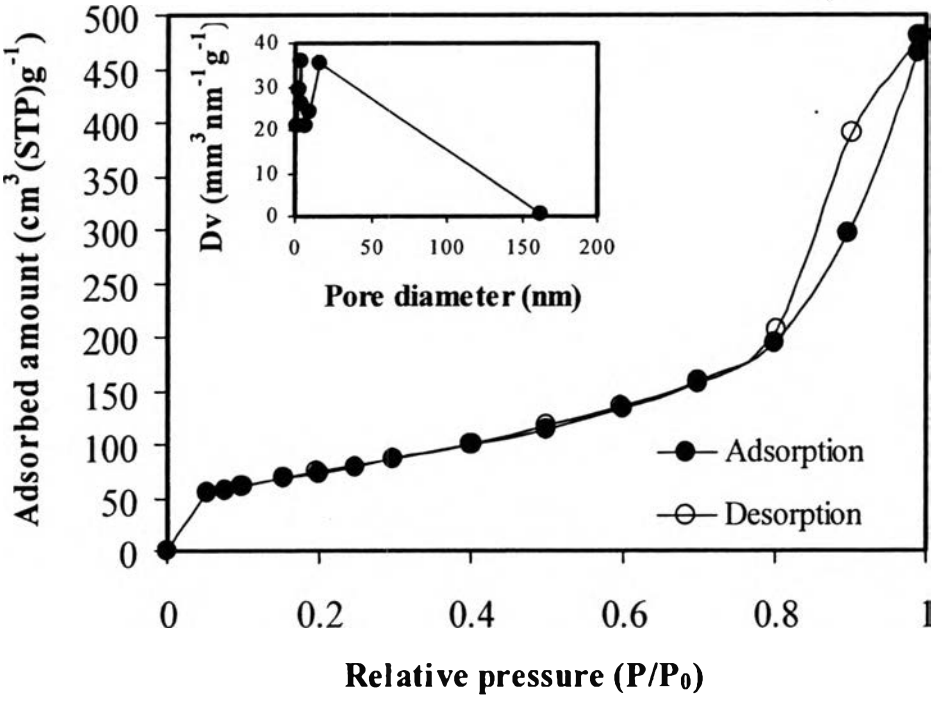

Figure 4.5 N_2 adsorption-desorption isotherms of the commercial ST-01 TiO_2 (Inset: Pore size distribution).

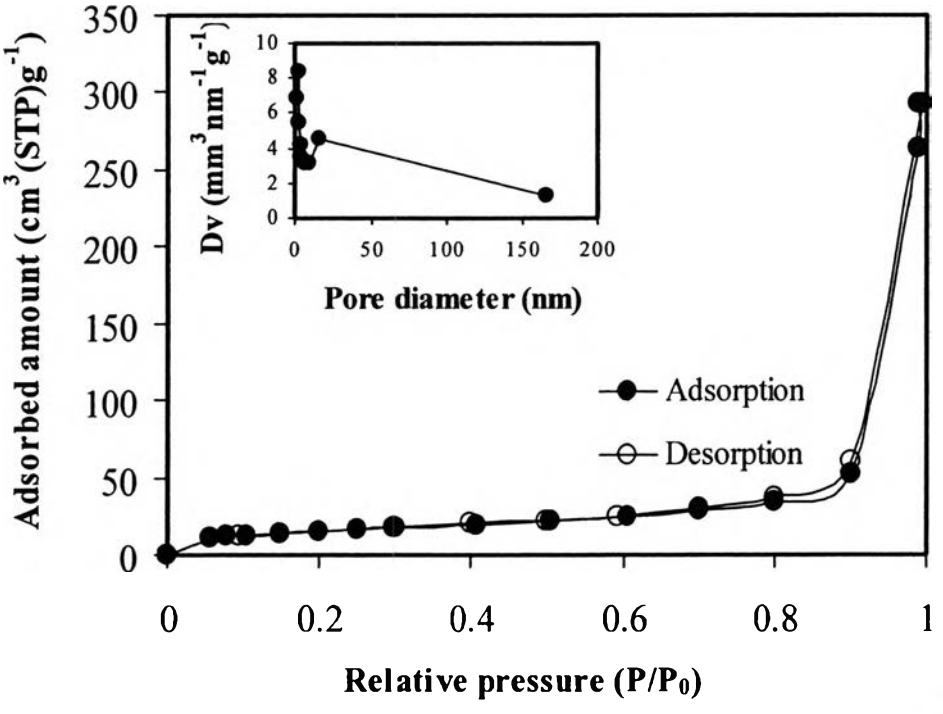

Figure 4.6 N_2 adsorption-desorption isotherms of the commercial JRC-03 TiO_2 (Inset: Pore size distribution).

The experimental results on textural properties of all investigated photocatalysts, including BET surface area, mean pore diameter, and total pore volume, are shown in Table 4.2. For the synthesized mesoporous-assembled TiO_2 photocatalysts, the increase in calcination temperature caused the decreases in surface area and total pore volume and the increase in mean pore diameter, as expected. For the commercial TiO_2 photocatalysts, whose isotherms exhibited IUPAC type II pattern, the mean pore diameter and total pore volume are always not reported because they contain a large portion of macropore, which possesses very broad pore size distribution with the pore diameter larger than 50 nm, up to 200 nm. Therefore, the surface area of P-25 TiO_2 and JRC-03 TiO_2 were consequently observed to be less than the synthesized mesoporous-assembled TiO_2 calcined at 500°C for 4 h, as shown in Table 4.2. However, the surface area of ST-01 TiO_2 was observed to be higher than the synthesized mesoporous-assembled TiO_2, plausibly resulting from its unique production process.

Table 4.2 Summary of textural properties obtained from N_2 adsorption-desorption results of the synthesized mesoporous-assembled TiO_2 and commercial TiO_2 photocatalysts

Photocatalyst	Calcination temperature (°C)	Calcination time (h)	BET surface area (m^2g^{-1})	Mean pore diameter (nm)	Total pore volume (cm^3g^{-1})
Mesoporous-assembled TiO_2	500	4	84.3	6.18	0.158
	600	4	22.7	8.83	0.061
	700	4	9.0	-[a]	-[a]
P-25 TiO_2	-	-	65.0	-[a]	-[a]
ST-01 TiO_2	-	-	289.5	-[a]	-[a]
JRC-03 TiO_2	-	-	55.0	-[a]	-[a]

[a] N_2 adsorption-desorption isotherms correspond to IUPAC type II pattern.

4.1.3 X-ray Diffraction Analysis

The XRD patterns of the synthesized mesoporous-assembled TiO_2 calcined at different temperatures, as compared with the commercial TiO_2 photocatalysts, are shown in Figure 4.7. Table 4.3 also summarizes all results of XRD analysis, including crystalline phase, rutile ratio, and crystallite size. The XRD patterns of the synthesized mesoporous-assembled TiO_2 samples calcined at 500 and 600°C show crystalline structure of pure anatase phase. The dominant peaks at 2θ about 25.2, 37.9, 47.8, 53.8, and 55.0°, which represent the indices of (101), (004), (200), (105), and (211) planes (JCPDS Card No. 21-1272), (Smith, 1960), respectively, are conformed to crystalline structure of anatase TiO_2. At calcination temperature of 700°C, partial phase transformation from anatase to rutile was observed, resulting in the combination of anatase and rutile phases. The occurrence of the dominant peaks at 2θ about 27.4, 36.1, 41.2, and 54.3°, which correspond to the indices of (110), (101), (111), and (211) planes (JCPDS Card No. 21-1276), (Smith, 1960), respectively, indicates the presence of rutile phase in the mesoporous-assembled TiO_2 calcined at this temperature. The main difference between mesoporous-assembled TiO_2 and commercial P-25 TiO_2 photocatalysts was that the commercial P-25 TiO_2 possesses mixed phase of anatase (74%) and rutile (26%), of which the phase composition was calculated by Equations (16) and (17) (Spurr and Myers, 1957). For ST-01 TiO_2 and JRC-03 TiO_2, they possess pure crystalline structure of anatase and rutile phase, respectively.

$$W_R = [1+0.8I_A/I_R]^{-1} \quad (23)$$

$$W_A = 1 - W_R \quad (24)$$

where I_A and I_R represent integrated intensities of anatase (101) and rutile (110) diffraction peaks, respectively, and W_A and W_R represent phase compositions of anatase and rutile, respectively.

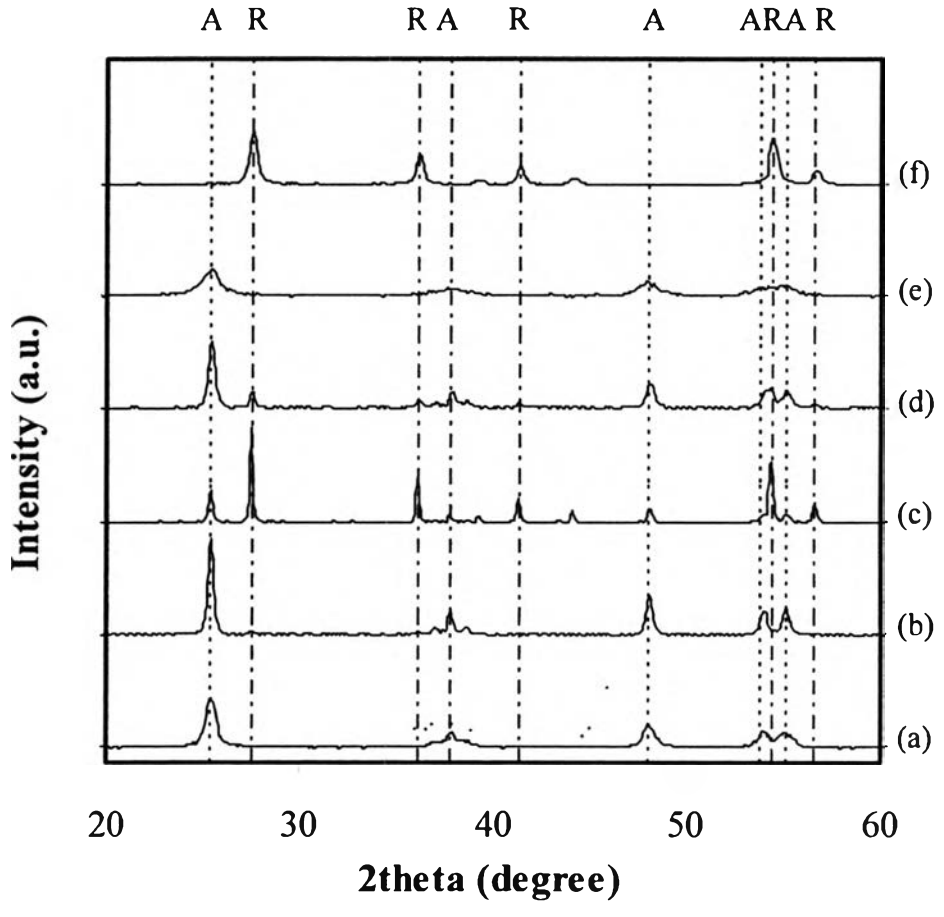

Figure 4.7 XRD patterns of synthesized mesoporous-assembled TiO_2 calcined at (a) 500°C, (b) 600°C, (c) 700°C, and commercial TiO_2 (d) P-25, (e) ST-01, and (f) JRC-03 (A=Anatase, R=Rutile).

Table 4.3 Summary of XRD analysis of the synthesized mesoporous-assembled TiO_2 calcined at different temperatures and commercial TiO_2

Photocatalyst	Calcination temperature (°C)	Calcination time (h)	Phase from XRD pattern	Rutile ratio (W_R)	Crystallite size (nm)	
					Anatase (101)	Rutile (110)
Mesoporous-assembled TiO_2	500	4	Anatase	-	13.64	-
	600	4	Anatase +Rutile	0.05	25.75	46.26
	700	4	Anatase +Rutile	0.79	38.75	53.96
P-25 TiO_2	-	-	Anatase +Rutile	0.26	22.01	28.90
ST-01 TiO_2	-	-	Anatase	-	8.33	-
JRC-03 TiO_2	-	-	Rutile	1	-	17.11

4.1.4 UV-Vis Spectroscopy

UV-Vis spectroscopy was used to investigate the light absorption capability of the photocatalysts. The UV-Vis spectra of the synthesized mesoporous-assembled TiO_2 photocatalyst calcined at different temperatures and the commercial TiO_2 photocatalysts are shown in Figure 4.8. The corresponding absorption wavelength and band gap energy are also summarized in Table 4.4.

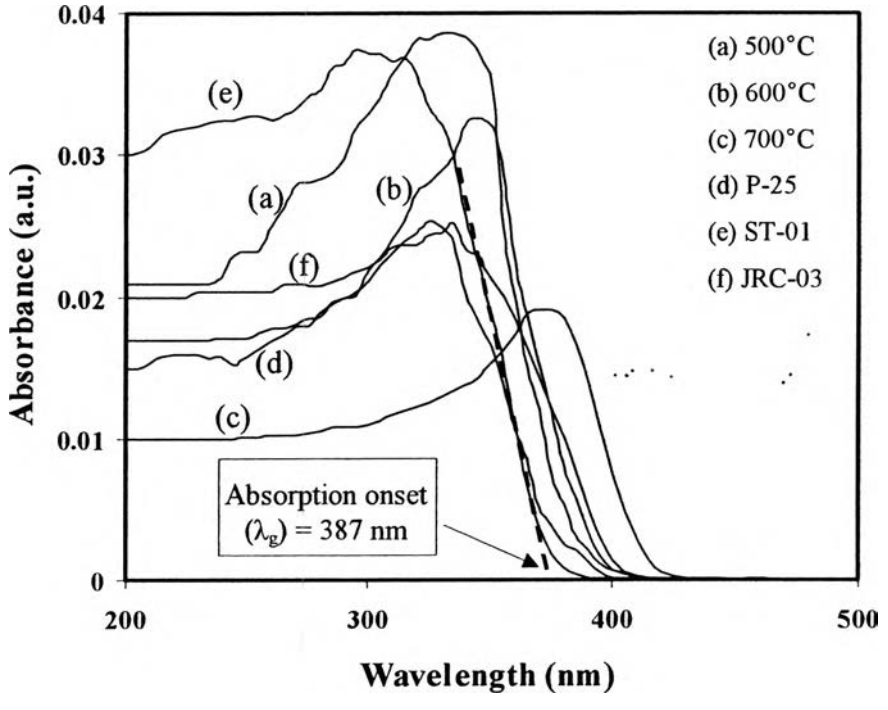

Figure 4.8 UV-Vis spectra of synthesized mesoporous-assembled TiO_2 photocatalyst calcined at (a) 500°C, (b) 600°C, and (c) 700°C for 4 h and commercial TiO_2 photocatalyst (d) P-25 TiO_2, (e) ST-01 TiO_2, and (f) JRC-03 TiO_2.

The energy band gap (E_g, eV) is determined by extrapolating the absorption onset of the rising part to x-axis (λ_g, nm) of the plots as shown by the dotted line in Figure 4.8 and calculating by Equation (18):

$$E_g = 1240/\lambda_g \qquad (25)$$

From Figure 4.8, the absorption band of all TiO_2 photocatalysts is approximately in the range of 200-400 nm. The strong absorption band at low wavelength in the spectra indicated the presence of Ti species as tetrahedral Ti^{4+}. This absorption band is generally associated with the electronic excitation of the valence band O2p electron to the conduction band Ti3d level (Fuerte *et al.*, 2002). The absorption onset is approximately at 387 nm for the synthesized mesoporous-assembled TiO_2 calcined at 500°C, which corresponds to the band gap energy of anatase TiO_2 of 3.2 eV. For the synthesized mesoporous-assembled TiO_2 calcined at 600°C, the absorption band shifts to wavelength 390 nm, which is correlated to the band gap energy of mixed anatase and rutile TiO_2 between 3.0-3.2 eV, whereas the absorption band of the synthesized mesoporous-assembled TiO_2 calcined at 700°C further shifts to wavelength longer than 400 nm, which is correlated to the band gap energy of rutile TiO_2 of 3.02 eV. For the commercial TiO_2 photocatalysts, their band gap energy reported in Table 4.4 also well corresponds to their crystalline phase obtained from XRD analysis (Figure 4.7). As comparatively seen from Figure 4.8, it is also perceptible that the light absorption capability of anatase TiO_2 at near UV region is significantly higher than that of rutile TiO_2.

Table 4.4 Summary of band gap energy obtained from UV-Vis spectra of the photocatalysts

Photocatalyst	Calcination temperature (°C)	Absorption wavelength, λ_g (nm)	Band gap energy (eV)
Mesoporous-assembled TiO_2	500	387	3.20
	600	390	3.18
	700	410	3.02
P-25 TiO_2	-	395	3.14
ST-01 TiO_2	-	385	3.22
JRC-03 TiO_2	-	410	3.02

4.1.5 SEM and TEM Analysis

Typical SEM and TEM images (for both low and high magnifications) of all investigated photocatalysts are shown in Figures 4.9, 4.10, and 4.11, respectively. SEM images of synthesized mesoporous-assembled TiO_2 indicate that the TiO_2 nanoparticles have reasonably uniform size with some nanoagglomeration of many crystallites. The presence of mesopore could be clearly observed by SEM analysis. In addition, TEM image demonstrates the formation of highly crystalline TiO_2 aggregates composed of three-dimensional disordered primary nanoparticles. The average size of the mesoporous-assembled TiO_2 nanoparticle calcined at 500°C is approximately 10-15 nm, which is consistent with the crystallite size estimated from XRD analysis. Therefore, each particle observed by TEM analysis should be a single crystal. For the commercial TiO_2 photocatalysts, SEM images also show the agglomeration of many particles; however, the

segregation of agglomerated particles seems to be quite evident than the mesoporous-assembled TiO_2, resulting in the presence of significant content of macropore as determined by the pore size distribution analysis. Moreover, the particle sizes of all commercial TiO_2 observed by TEM analysis agree well with the crystallite sizes calculated from their XRD patterns.

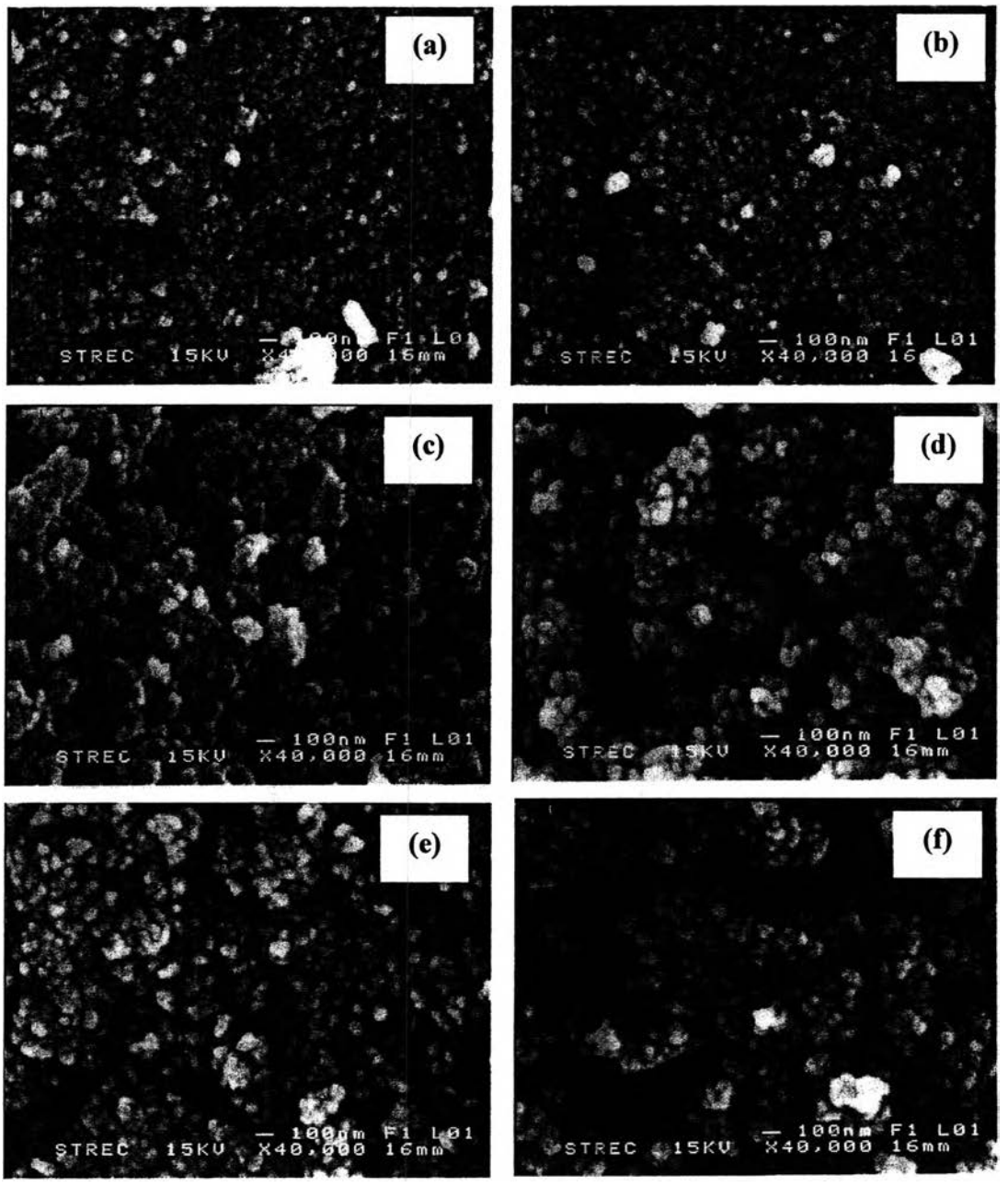

Figure 4.9 SEM images of synthesized mesoporous-assembled TiO_2 calcined at (a) 500°C, (b) 600°C, (c) 700°C, and commercial TiO_2 (d) P-25 TiO_2, (e) ST-01 TiO_2, and (f) JRC-03 TiO_2.

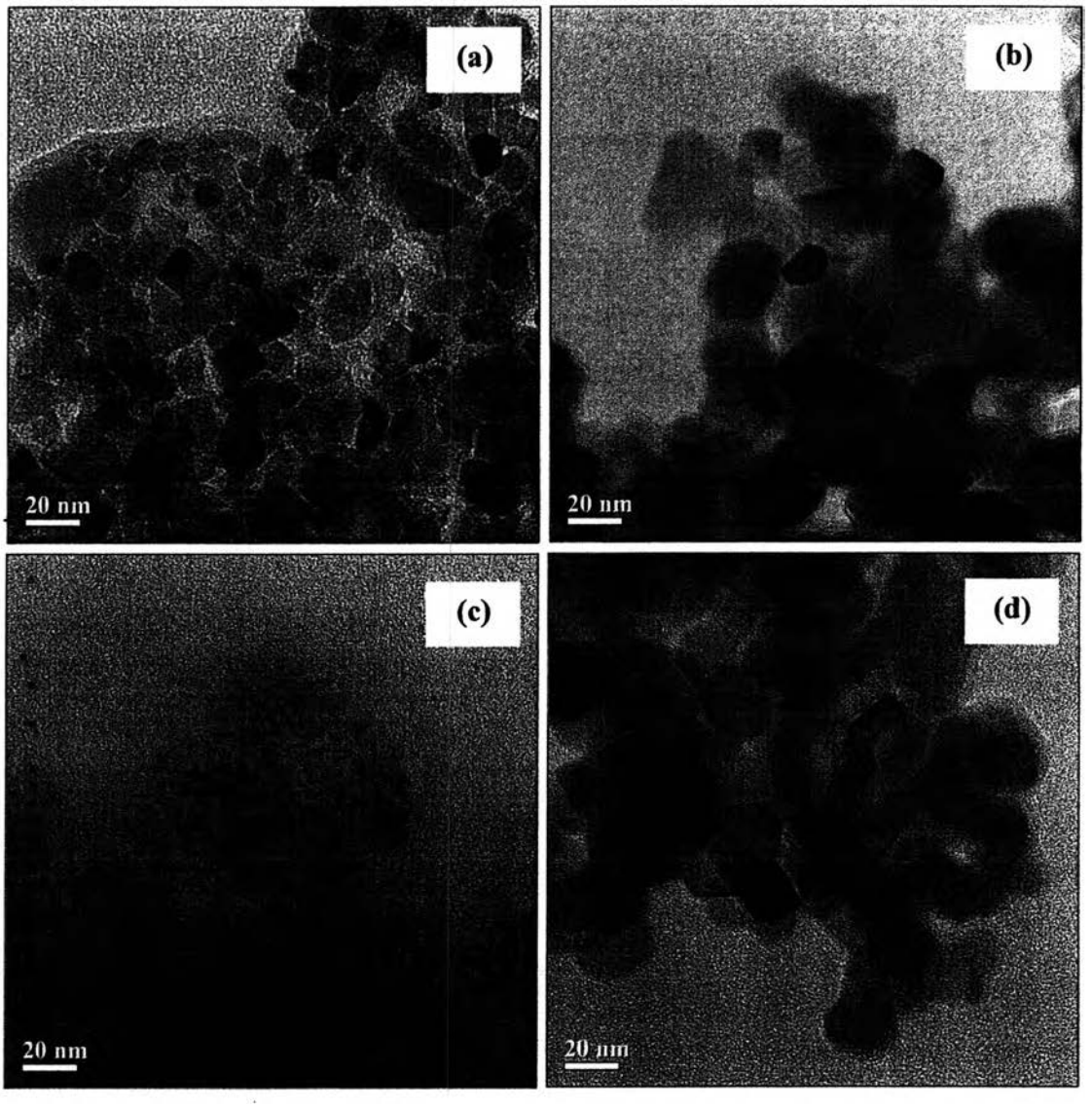

Figure 4.10 TEM images (low magnification) of synthesized mesoporous-assembled TiO_2 calcined at (a) 500°C, and commercial TiO_2 (b) P-25 TiO_2 (c) ST-01 TiO_2, and (d) JRC-03 TiO_2.

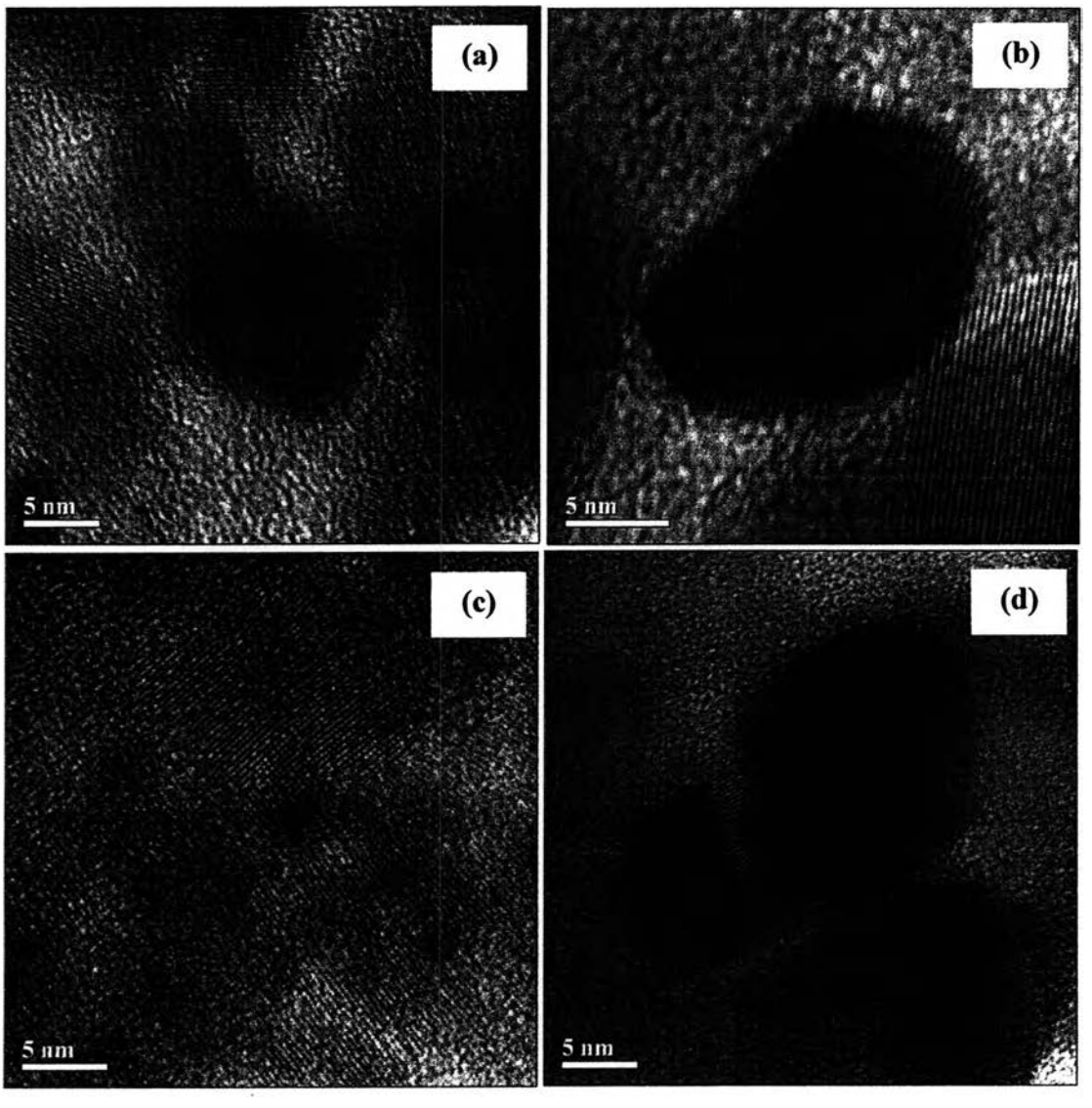

Figure 4.11 TEM images (high magnification) of synthesized mesoporous-assembled TiO_2 calcined at (a) 500°C, and commercial TiO_2 (b) P-25 TiO_2 (c) ST-01 TiO_2, and (d) JRC-03 TiO_2.

4.2 Photocatalytic MO Decomposition Results of TiO_2 Photocatalysts

The UV-Vis spectrum of MO solution shows two absorption maxima, as shown in Figure. 4.12, with the first band centered at 270 nm and the second band at 465 nm. In this work, the absorbance at 465 nm is due to $\pi \rightarrow \pi^*$ transition of –N=N– group, representing the color of dye solution, and its decrease was used to monitor the decolorization of MO dye. The absorbance at 270 nm is due to $\pi \rightarrow \pi^*$ transition in benzene group, representing the aromatic content of methyl orange, and its decrease was used to monitor the degradation of aromatic part of MO dye. Selvam *et al.* (2005) also explained about the photocatalytic decolorization and degradation of a chlorotriazine reactive azo dye, Reactive Orange 4 (RO4), of which two corresponding absorption maxima occurs at 489 nm and 285 nm, respectively. Therefore, in this study, both the decolorization and degradation (referred as decomposition in overall) of MO dye in terms of relative concentration (C/C_0) and reaction rate constant were investigated.

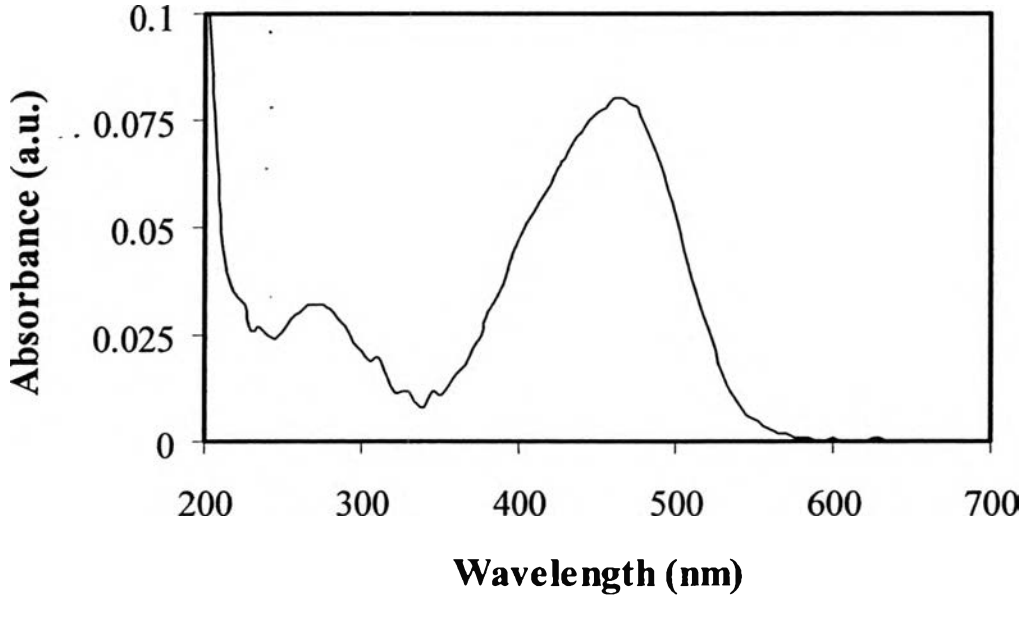

Figure 4.12 UV-Vis absorption spectrum of methyl orange solution.

In addition, Hanchem *et al.* (2001) pointed out that the adsorption of Reactive Orange 4 (RO4) on commercial TiO_2 photocatalyst was quite fast, and the adsorption/desorption equilibrium could be reached within about 45 min. In this work, the adsorption equilibrium of the photocatalyst/MO solution suspensions was established by being magnetically stirred in a dark condition for 1 h.

4.2.1 Effect of Photocatalyt Type

In this work, two main types of photocatalysts used for studying the photocatalytic decomposition of methyl orange (MO) were the synthesized mesoporous-assembled TiO_2 calcined at 500, 600, and 700°C and the non-mesoporous-assembled commercial TiO_2 (P-25 TiO_2, ST-01 TiO_2, and JRC-03 TiO_2). It must be first noted that no appreciable MO decomposition was detected in the absence of either light irradiation or photocatalyst. The results of photocatalytic decolorization and degradation of MO over various types of TiO_2 photocatalysts are shown in Figure 4.13(a) and (b), respectively. The results show that the synthesized mesoporous-assembled TiO_2 calcined at 500°C gave the highest efficiency in both the decolorization and degradation due to the most rapid decrease in their concentrations. The photocatalytic decomposition of MO solution is proved to be pseudo-first-order reaction, and its kinetics can be expressed as $\ln(C_0/C) = kt$. The calculated reaction rate constants (k) of each type of photocatalyst from Figure 4.13(a) and (b) are listed in Table 4.5.

As shown in Table 4.5, the rate constants of synthesized mesoporous-assembled TiO_2 for both decolorization and degradation decreased with increasing calcination temperature. This might be because of the observed loss in surface area, shown in Table 4.2, which is attributable to pore coalescence due to the crystallization of walls separating mesopores as previously explained. Consequently, this tendency caused lower surface active reaction site and higher probability of mutual e^-/h^+ recombination, leading to lower photocatalytic activity. Moreover, it can be noticed that the increasing rutile content in the synthesized TiO_2 photocatalyst calcined at higher temperature negatively affected the photocatalytic decomposition of MO, probably due to the lower flat band level of rutile than anatase phase (lower band gap energy).

For P-25 TiO_2, the phase combination between anatase and rutile (rutile ratio of 0.26, as shown in Table 4.3) and lower BET surface area than that of the synthesized mesoporous-assembled TiO_2 calcined at 500°C might be the causes of very low photocatalytic activity. Despite large surface area about 290 m^2g^{-1} of ST-01 TiO_2, its imperfect crystallization from XRD (Figure 4.7) accompanying with fairly small crystallite size (Table 4.3) is considered to increase the probability of mutual e^-/h^+ recombination at both surface and bulk traps. In case of JRC-03 TiO_2, it possesses only rutile TiO_2 phase, therefore giving the lowest reaction rate. Moreover, lack of mesoporous structure in these three commercial TiO_2 powders (as shown in Table 4.2 and Figure 4.9) is also subjected to less reactant accessibility for the photocatalytic reaction. In contrast, the use of the nanocrystalline mesoporous-assembled TiO_2 with uniform pore size and high crystallinity could decrease the number of lattice defects and then facilitate the electron and hole transport for reacting with water and/or oxygen molecules adsorbed at TiO_2 surface along the mesoporous structure to create many active species, such as $OH^{\bullet}$ and $O_2^{\bullet-}$. As a consequence of these results, the mesoporosity has been proved to be very important property of TiO_2 photocatalyst.

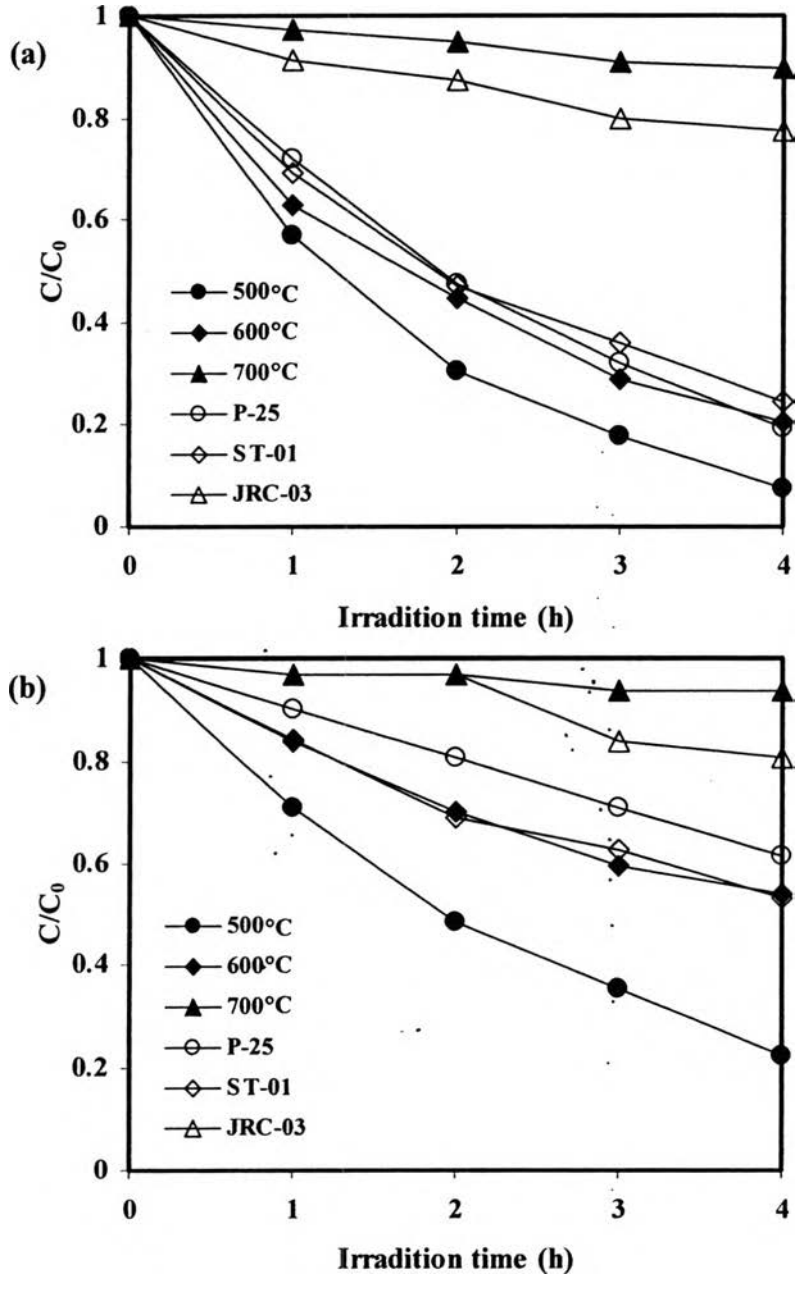

Figure 4.13 Effect of photocatalyst type on relative concentration (C/C_0) for (a) decolorization and (b) degradation of MO by synthesized mesoporous-assembled TiO_2 photocatalyst calcined at various temperatures (500, 600, and 700°C) and commercial TiO_2 photocatalyst as a function of irradiation time (photocatalyst dosage = 0.2 g/l; initial MO concentration = 5 mg/l; reaction volume = 80 ml).

Table 4.5 Comparison of effect of photocatalyst type on reaction rate constants for both decolorization and degradation of MO by synthesized mesoporous-assembled TiO_2 photocatalyst calcined at various temperatures and commercial TiO_2 photocatalyst (photocatalyst dosage = 0.2 g/l; initial MO concentration = 5 mg/l; reaction volume = 80 ml; irradiation time = 4 h)

Photocatalyst	Calcination temperature (°C)	Reaction rate constant, k (h^{-1})	
		Decolorization	Degradation
Mesoporous-assembled TiO_2	500	0.615	0.362
	600	0.405	0.163
	700	0.029	0.019
P-25 TiO_2	-	0.394	0.117
ST-01 TiO_2	-	0.352	0.162
JRC-03 TiO_2	-	0.068	0.050

4.2.2 Effect of Photocatalyst Dosage

The effect of TiO_2 photocatalyst dosage on the photocatalytic decomposition of MO dye was next investigated. The results of photocatalytic decolorization and degradation of MO using various photocatalyst dosages of synthesized mesoporous-assembled TiO_2 calcined at 500°C, exhibiting the best photocatalytic activity among all investigated TiO_2 photocatalysts, are shown in Figure 4.14(a) and (b), respectively. The calculated reaction rate constants (k) at each photocatalyst dosage from Figure 4.14(a) and (b) are also presented in Figure 4.15.

From Figure 4.15, the results indicate that significant increases in the photocatalytic decomposition rates were observed when the photocatalyst dosage was increased to 7 g/l. However, when it exceeded 7 g/l, the photocatalytic decomposition rate constants adversely decreased. The photocatalytic decolorization and degradation rates at this optimum photocatalyst dosage value of 7 g/l for the mesoporous-assembled TiO_2 nanoparticle were 1.07 and 0.68 h^{-1}, respectively. On the basis of the relevant band gap absorption of the investigated photocatalyst dosage, the results can be explained in terms of the availability of active sites on the TiO_2 surfaces, the light absorption, and the penetration depths into the suspension. With increasing the photocatalyst dosage until reaching the optimum value, the TiO_2 surface active sites, as well as absorption ability of TiO_2, accordingly increased. On the other hand, under the higher photocatalyst dosage, there was still only a small portion of productive particles near the photoreactor wall that can completely absorb the incident light. This means that at high photocatalyst dosage, the photocatalyst has high tendency to be agglomerated, and therefore low amount of the photocatalyst can absorb the irradiated light. Furthermore, the light penetration depths become less due to the agglomeration and sedimentation of particles under a higher photocatalyst dosage, which could result in the light scattering, thus dramatically reducing the intensity of light entering the irradiated suspension.

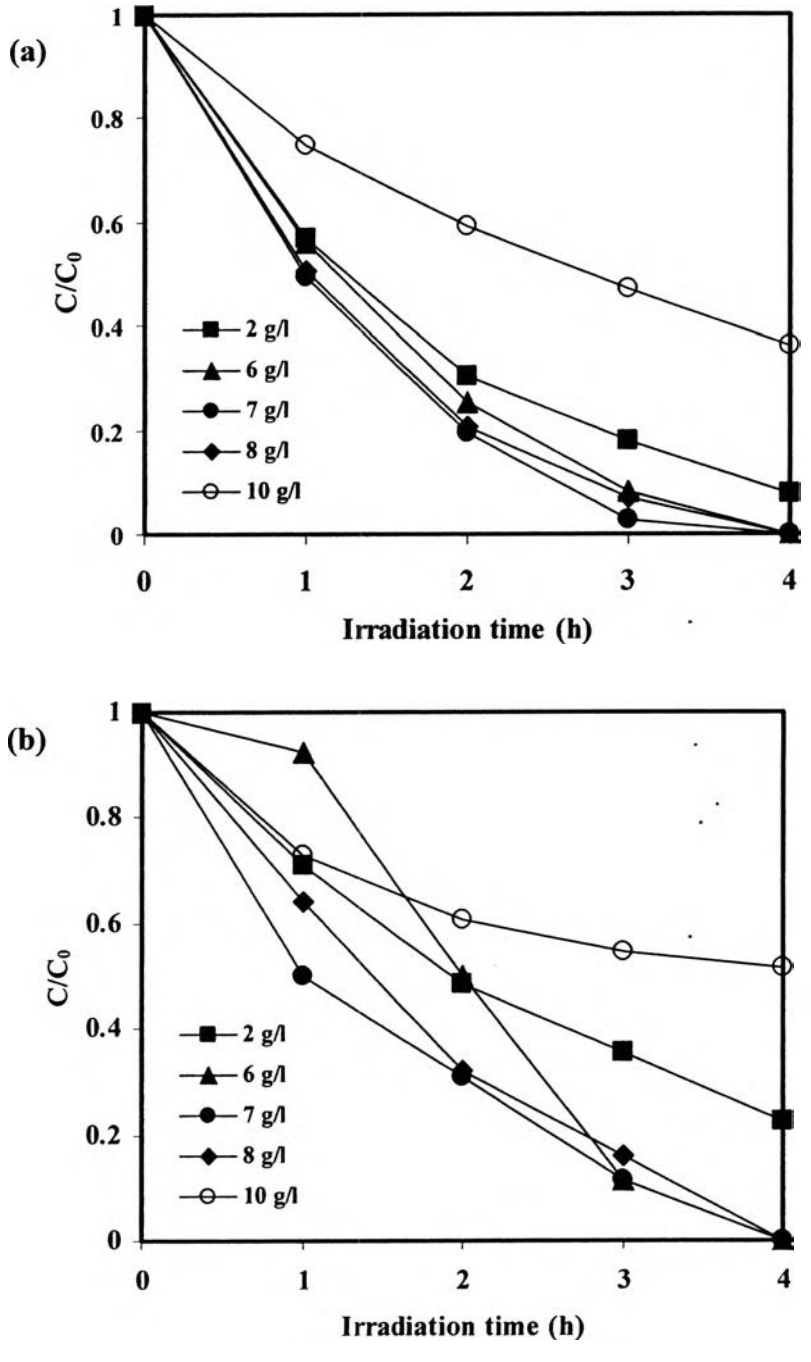

Figure 4.14 Effect of photocatalyst dosage on relative concentration (C/C_0) for (a) decolorization and (b) degradation of MO by synthesized mesoporous-assembled TiO_2 photocatalyst calcined at 500°C as a function of irradiation time (initial MO concentration = 5 mg/l; reaction volume = 80 ml).

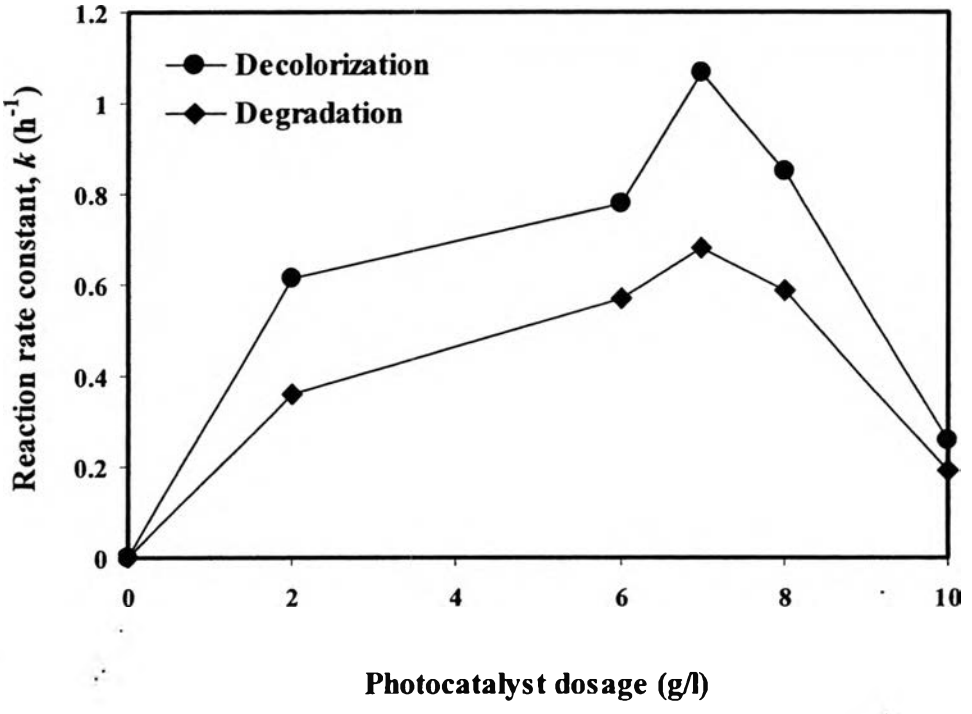

Figure 4.15 Effect of photocatalyst dosage on reaction rate constants for (a) decolorization and (b) degradation of MO by synthesized mesoporous-assembled TiO_2 photocatalyst calcined at 500°C (initial MO concentration = 5 mg/l; reaction volume = 80 ml; irradiation time = 4 h).

4.2.3 Effect of Initial MO Concentration

From literature, it was found that the decomposition rate of azo dye increased with the increase in dye concentration to a certain level, and a further increase in dye concentration leads to decrease the decomposition rate of the dye. In this work, different initial MO concentrations ranging from 2.5-15 mg/l were used to study the effect of initial MO concentration to find its optimum for the synthesized mesoporous-assembled TiO_2 photocatalyst. The photocatalytic decolorization and degradation of MO at various initial MO concentrations of the synthesized mesoporous-assembled TiO_2 calcined at 500°C are depicted in Figure 4.16(a) and (b), and the calculated reaction rate constants (k) at each initial MO concentration from Figure 4.16(a) and (b) are shown in Figure 4.17.

From Figure 4.17, the decomposition rates (both decolorization and degradation) of MO increased with increasing initial MO concentration from 2.5 to 5 mg/l and decreased when further increasing initial MO concentration from 5 to 15 mg/l. The rates of decomposition strongly relate to the probability of $OH^{\bullet}$ radical formation on the photocatalyst surface and also relate to the probability of $OH^{\bullet}$ radicals reacting with dye molecule (Konstantinou *et al.*, 2004). When the initial MO concentration is increased, the probability of reaction between dye molecule and oxidizing species also increases, leading to an enhancement in the decolorization and degradation rates. However, the decomposition efficiency of the MO molecule decreases as the MO concentration is further increased. The reason may be because at high initial MO concentrations, the generation of $OH^{\bullet}$ radicals on the surface of photocatalyst is reduced since the active sites are covered by dye ions. Another possible cause for these results is the significant absorption of light by the MO dye molecule itself instead of that by the photocatalyst, and this reduces the efficiency of the photocatalytic reaction because the concentrations of $OH^{\bullet}$ and $O_2^{\bullet-}$ decrease (Konstantinou *et al.*, 2004). Therefore, it can be concluded that the suitable initial MO concentration for the photocatalytic reaction of the mesoporous-assembled TiO_2 calcined at 500°C with 7 g/l photocatalyst dosage was 5 mg/l.

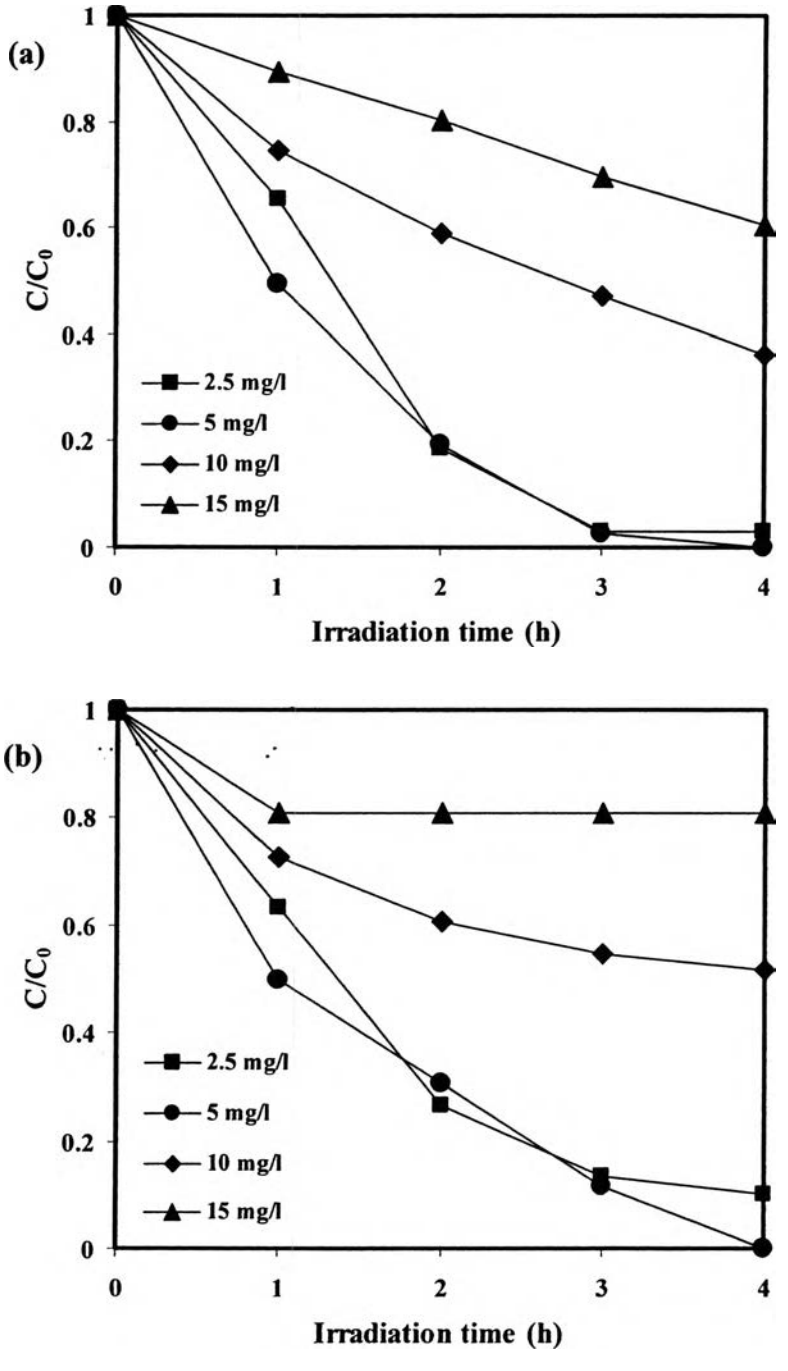

Figure 4.16 Effect of initial MO concentration on relative concentration (C/C_0) for (a) decolorization and (b) degradation of MO by synthesized mesoporous-assembled TiO_2 photocatalyst calcined at 500°C as a function of irradiation time (photocatalyst dosage = 7 g/l; reaction volume = 80 ml).

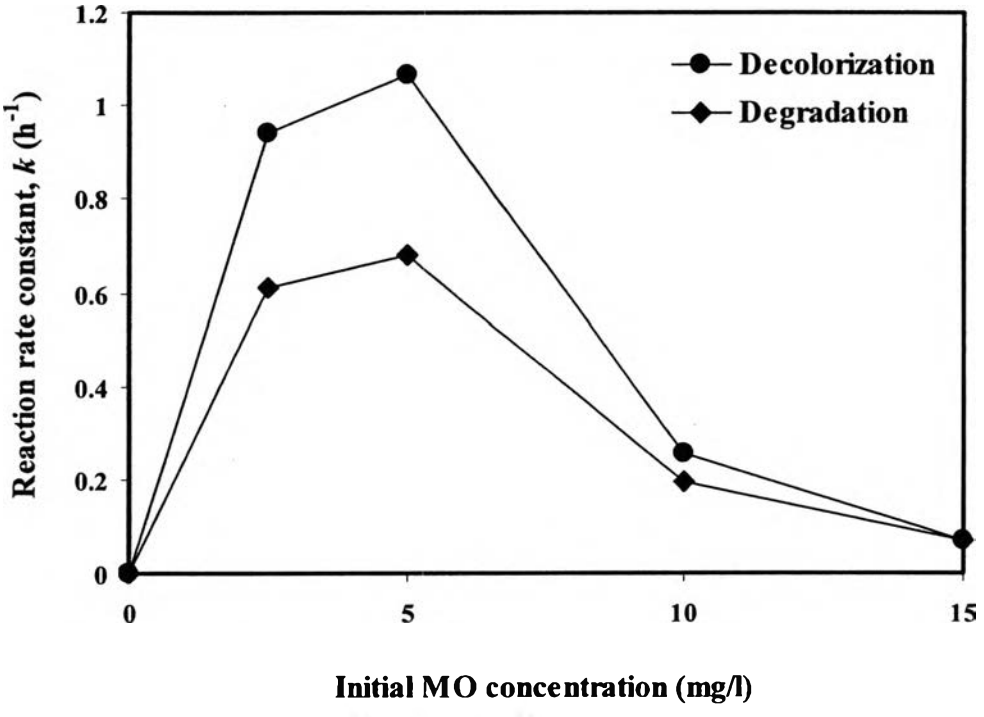

Figure 4.17 Effect of initial MO concentration on reaction rate constants for (a) decolorization and (b) degradation of MO by synthesized mesoporous-assembled TiO_2 photocatalyst calcined at 500°C (photocatalyst dosage = 7 g/l; reaction volume = 80 ml; irradiation time = 4 h).

4.2.4 Effect of Light Intensity

Figure 4.18(a) and (b) show the photocatalytic decolorization and degradation of MO at various light intensities (0.58-2.32 mW/cm^2) of synthesized mesoporous-assembled TiO_2 calcined at 500°C, and the calculated reaction rate constants (k) at each light intensity from Figure 4.18(a) and (b) are shown in Figure 4.19. The maximum light intensity of 2.32 mW/cm^2 was employed in this study in order to control the temperature of reaction mixture to be less than 60°C. The results from Figure 4.19 show the increase in photocatalytic decolorization and degradation rates when increasing the light intensity, as expected. These results agree well with the work of Ollis *et al.* (2004) reporting that at low light intensities (0-20 mW/cm^2), the decomposition rate of cationic triarylmethane dyes (crystal violet and fuchsin basic) increased linerly with increasing light. This is likely because at low light intensity, reactions involving electron-hole formation are predominant, and electron-

hole recombination becomes negligible. It can also be noticed that at higher light intensity, the required decomposition time was decreased.

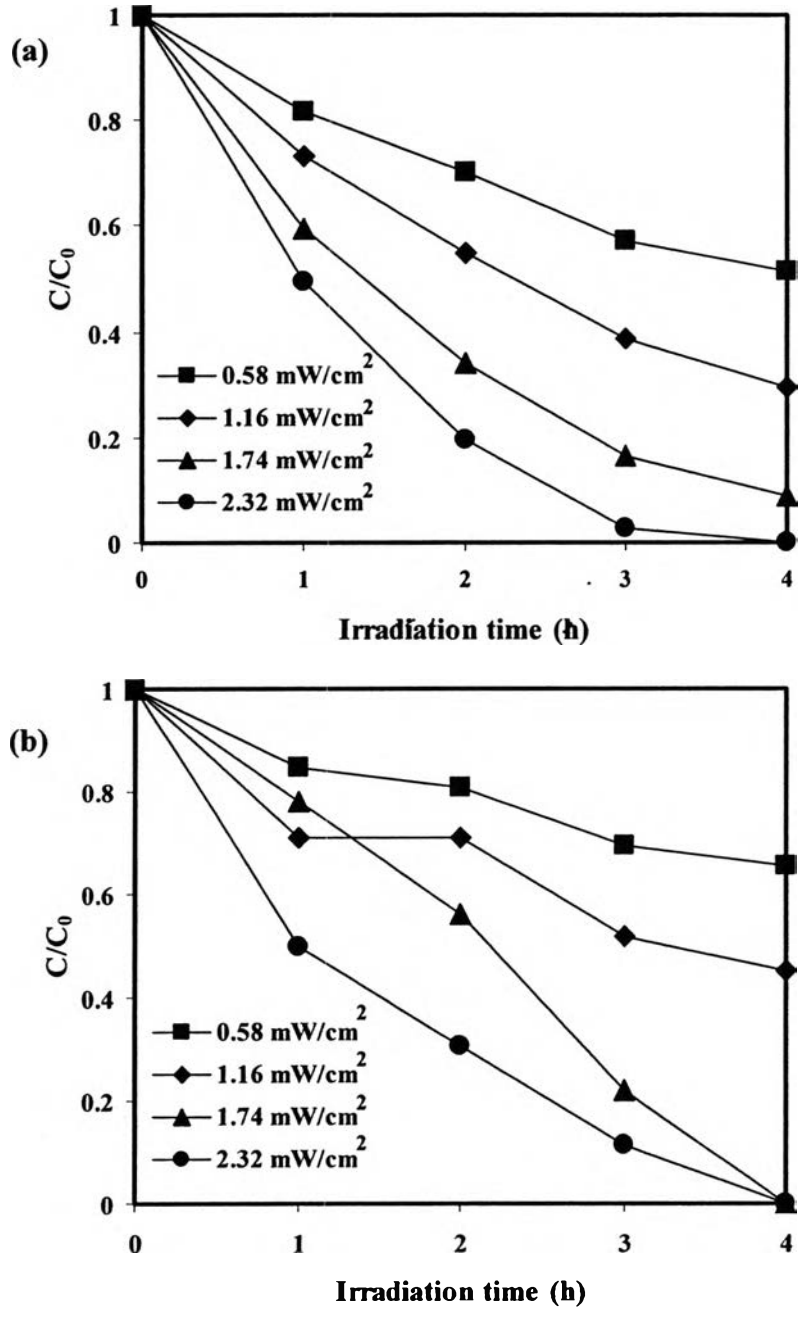

Figure 4.18 Effect of light intensity on relative concentration (C/C_0) for (a) decolorization and (b) degradation of MO by synthesized mesoporous-assembled TiO_2 photocatalyst calcined at 500°C as a function of irradiation time (initial MO concentration = 5 mg/l; photocatalyst dosage = 7 g/l; reaction volume = 80 ml).

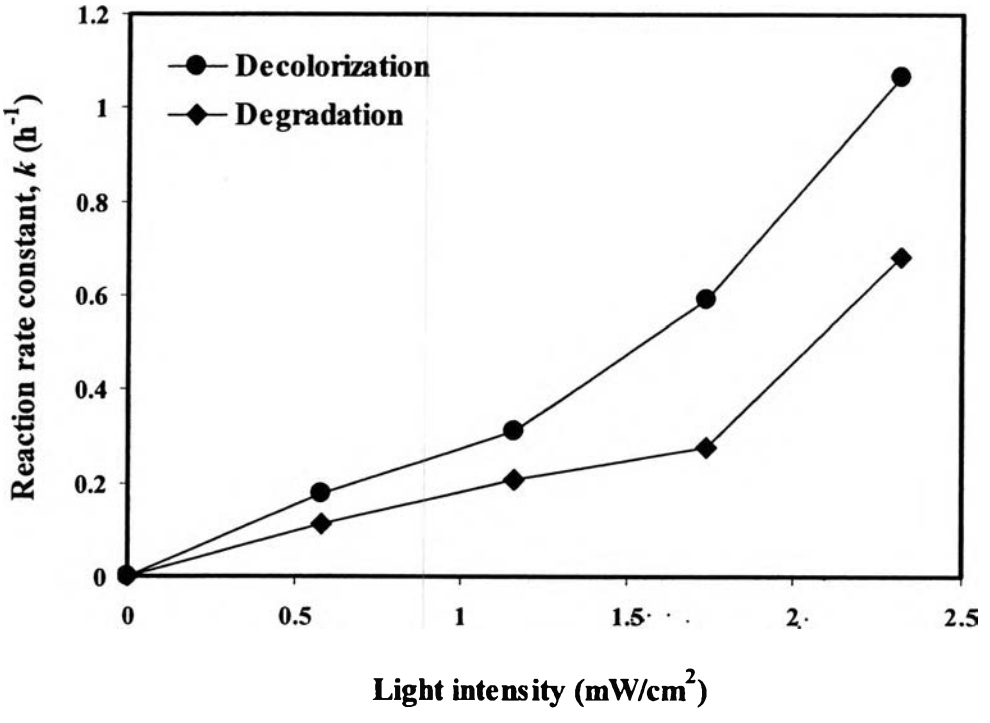

Figure 4.19 Effect of light intensity on reaction rate constants for (a) decolorization, and (b) degradation of MO by synthesized mesoporous-assembled TiO_2 photocatalyst calcined at 500°C (initial MO concentration = 5 mg/l; photocatalyst dosage = 7 g/l; reaction volume = 80 ml; irradiation time = 4 h).

4.2.5 Effect of H_2O_2 Concentration

In order to increase the photocatalytic decomposition rate of MO dye by the synthesized mesoporous-assembled TiO_2 nanoparticle calcined at 500°C, H_2O_2, which is a strong oxidant, was selected to add into the reaction suspension. Figure 4.20 shows the photocatalytic decolorization of MO over synthesized mesoporous-assembled TiO_2 calcined at 500°C at various H_2O_2 concentrations, and the calculated reaction rate constant (k) at each H_2O_2 concentration from Figure 4.20 is shown in Figure 4.21. Note that for the effect of H_2O_2 concentration, only the decolorization of MO due to the decrease in the absorbance peak centered at 465 nm could be determined and reported. Because the absorbance peak centered at 270 nm is significantly interfered by the added H_2O_2, the degradation of aromatic part of MO could not be examined. Moreover, it must be noted that the photodecomposition of MO dye in the system containing the photocatalyst and 0.5 M H_2O_2 (optimum value as shown later) but in the absence of light irradiation did not occur, whereas the decolorization rate constant of MO dye when using 0.5 M H_2O_2 with light irradiation but in the absence of photocatalyst was observed to only be 0.15 h^{-1}.

From Figure 4.21, when H_2O_2 concentration was increased from 0.1 to 0.5 M, the decolorization rate greatly increased. The gradual decrease in the decolorization rate was observed when further increasing H_2O_2 concentration from 0.5 to 0.9 M. The improved photocatalytic activity of mesoporous-assembled TiO_2 photocatalyst in the presence of H_2O_2 with the concentration up to 0.5 M is attributed to the reactive hydroxyl radical intermediate ($OH^{\bullet}$) formed from the oxidant by reaction with the photogenerated electrons. H_2O_2 can exert a dual function: as strong oxidant itself and as electron scavenger, thus inhibiting the electron-hole recombination at the semiconductor surface (Gratzel *et al.*, 1990). On the other hand, the photocatalytic decolorization rate decreased with further increasing H_2O_2 concentration to be higher than 0.5 M due to too high content of reactive $OH^{\bullet}$ radicals. The radical-radical recombination as a competitive reaction must be taken into account. In addition, if high amount of H_2O_2 adsorbs onto TiO_2 particles to modify their surface, the photocatalytic decolorization rate would be subsequently decreased (Sun *et al.*, 2007), probably due to the light screening effect of H_2O_2 itself to cause less photoexcitation of the photocatalyst.

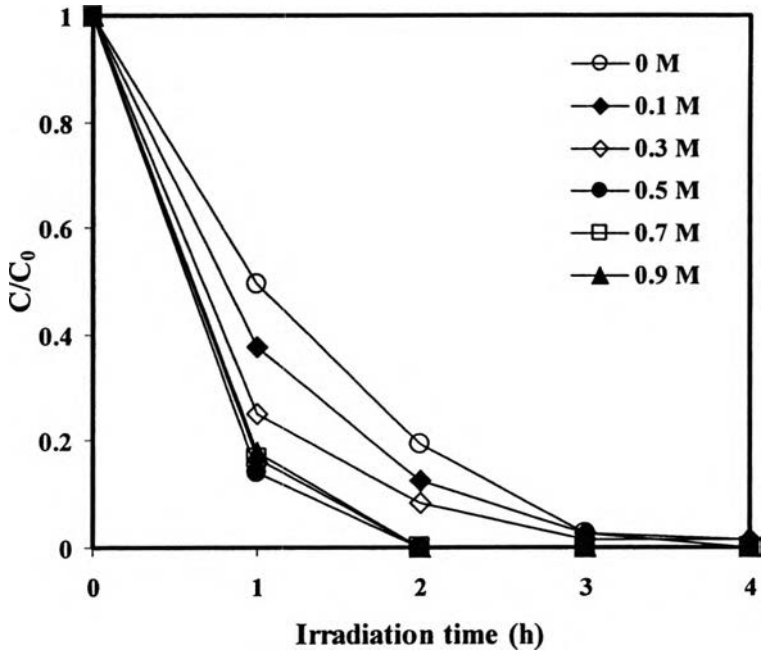

Figure 4.20 Effect of H_2O_2 concentration on relative concentration (C/C_0) for decolorization of MO by synthesized mesoporous-assembled TiO_2 photocatalyst calcined at 500°C as a function of irradiation time (initial MO concentration = 5 mg/l; photocatalyst dosage = 7 g/l; reaction volume = 80 ml).

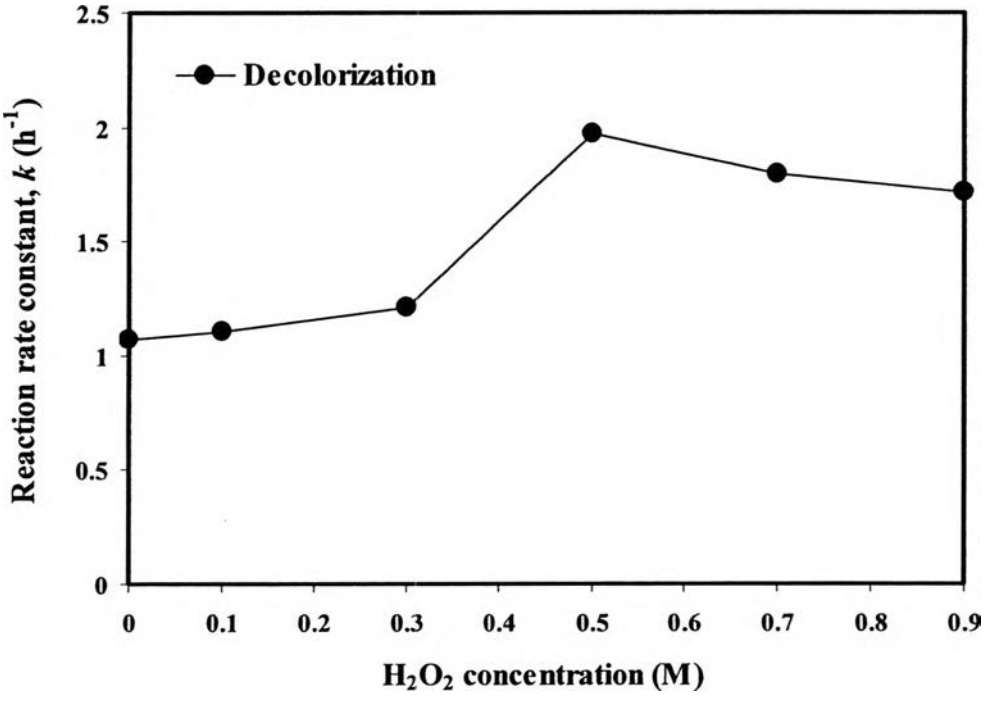

Figure 4.21 Effect of H_2O_2 concentration on reaction rate constant for decolorization of MO by synthesized mesoporous-assembled TiO_2 photocatalyst calcined at 500°C (initial MO concentration = 5 mg/l; photocatalyst dosage = 7 g/l; reaction volume = 80 ml; irradiation time = 4 h).

4.2.6 Effect of Initial Solution pH

The pH of solution is an important parameter in the photocatalytic processes, since it not only plays an important role on the characteristics of textile wastewater but also determines the surface charge properties of TiO_2, the size of aggregates formed, the charge of dye molecules, the adsorption of MO dye onto TiO_2 surface, and the concentration of hydroxyl radicals. In this work, both HCl and NaOH were used to adjust the MO solution pH in the range of 3-8. Figure 4.22 shows the photocatalytic decolorization of MO over the synthesized mesoporous-assembled TiO_2 calcined at 500°C at various solution pHs, and the calculated reaction rate constant (k) at each solution pH is shown in Figure 4.23. Note that only the decolorization of MO was reported due to the interference of pH-adjusting compounds on the low wavelength absorption band, as well.

The results indicate that the higher photocatalytic decolorization occurred at pH lower than point of zero charge (pzc) of TiO_2, which is about 6.0±0.3 (Parks, 1965). When MO dye is dissolved in water, its structure becomes negatively charged. In contrast, the surface of TiO_2 photocatalyst becomes positively charged when the solution pH is lower than its pzc. These opposite charges favorably lead to the enhancement of the photocatalytic decolorization due to their increased interaction. The optimum pH value for this reaction system was found at solution pH of 4.7. However, at lower pHs of 4.1 and 3.1, the photocatalytic decolorization decreased due to the plausible agglomeration of TiO_2 particles, which consequently reduces the surface area available for reactant adsorption and photon absorption. Moreover, at too low pH with the excess concentration of H^+, the H^+ ions interact with the azo link (-N=N-), which is particularly susceptible to be electrophilic attack by hydroxyl radical, leading to decreasing the electron densities at azo group. Consequently, the reactivity of hydroxyl radical by electrophilic mechanism decreases (Sun. *et al.*, 2007). At alkali solution pHs of 7.0 and 8.0, low photocatalytic decolorization rate was observed. At this condition, there was a coulombic repulsion between the negatively charged surface of photocatalyst and the negatively charge MO molecule, and therefore the photocatalytic decolorization process would be reduced (Konstantinou *et al.*, 2004).

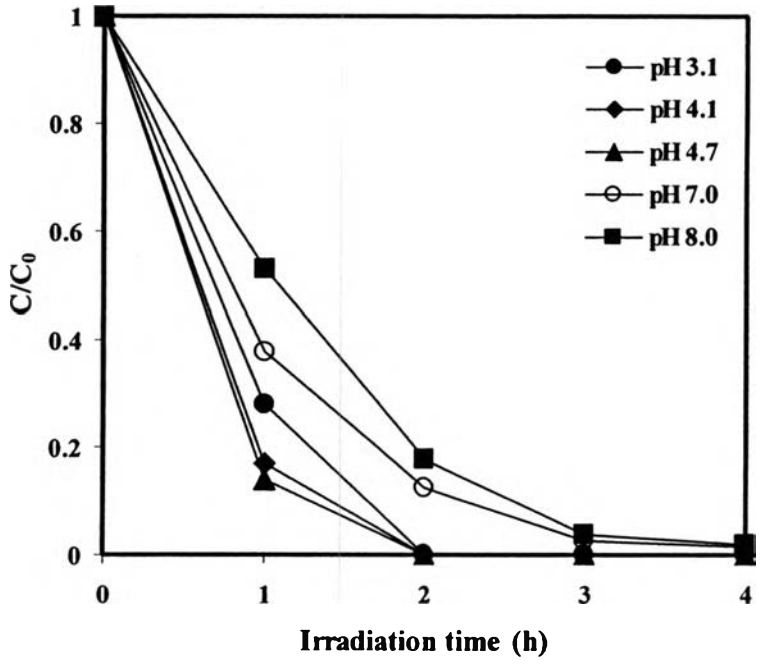

Figure 4.22 Effect of initial solution pH on relative concentration (C/C_0) for decolorization of MO by synthesized mesoporous-assembled TiO_2 photocatalyst calcined at 500°C as a function of irradiation time (initial MO concentration = 5 mg/l; photocatalyst dosage = 7 g/l; H_2O_2 concentration = 0.5 M; reaction volume = 80 ml).

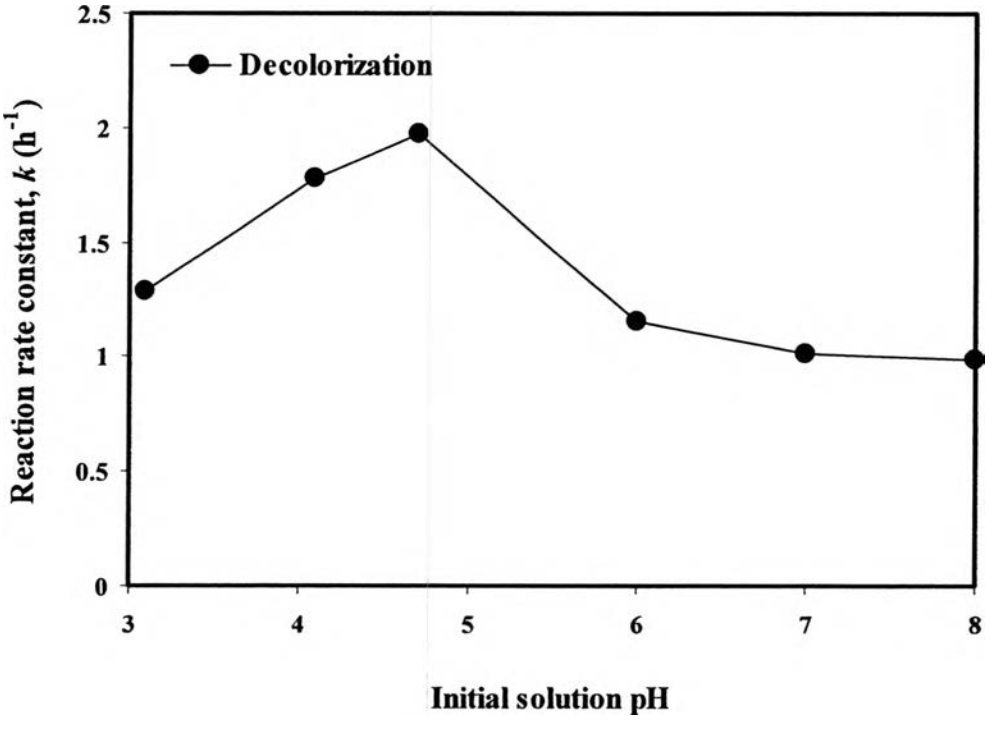

Figure 4.23 Effect of initial solution pH on reaction rate constant for decolorization of MO by synthesized mesoporous-assembled TiO_2 photocatalyst calcined at 500°C (initial MO concentration = 5 mg/l; photocatalyst dosage = 7 g/l; H_2O_2 concentration = 0.5 M; reaction volume = 80 ml; irradiation time = 4 h).

4.3 Characterization and Photocatalytic MO Decomposition Results of Pt-Loaded Mesoporous-Assembled TiO_2 Photocatalyst

In order to understand the role of Pt cocatalyst, the brief mechanism of photocatalytic decomposition of MO over Pt-loaded TiO_2 is first explained. The reaction is initiated by the photoexcitation of TiO_2 particles, which leads to the formation of electron-hole pairs. Photogenerated conduction band electrons can be transferred to O_2 electron acceptor to form active $O_2^{\bullet -}$ radical, which further reacts with H^+ to form active $HO_2^{\bullet}$ radical. With Pt on TiO_2 photocatalyst, Pt can rapidly trap electrons, which further undergo through such active radical formation, resulting in the great prevention of photoinduced charge recombination. In the meantime, valence band holes can then easily react with OH^- to form active $OH^{\bullet}$ radical (Konstantinou *et al.*, 2004 and Mahmoodi *et al.*, 2005). All of these active radicals are responsible for the MO decomposition.

Since among all the investigated photocatalysts, the mesoporous-assembled TiO_2 photocatalyst calcined at 500°C showed the highest photocatalytic activity, it was taken to study the effect of Pt cocatalyst loading content in order to improve the decomposition of MO. The Pt with various loading contents ranging from 0.2 to 0.8 wt.% was loaded onto the mesoporous-assembled TiO_2 photocatalyst by using the single step sol-gel method. The N_2 adsorption-desorption isotherms of the synthesized 0.6 wt.% Pt/TiO_2 photocatalyst calcined at 500°C, providing the best photocatalytic performance for MO decomposition as next discussed, also exhibited typical IUPAC type IV pattern (Rouquerol *et al.*, 1999), as shown in Figures 4.24. The experimental results on textural properties of all investigated Pt-loaded photocatalysts, including BET surface area, mean pore diameter, and total pore volume, are shown in Table 4.6.

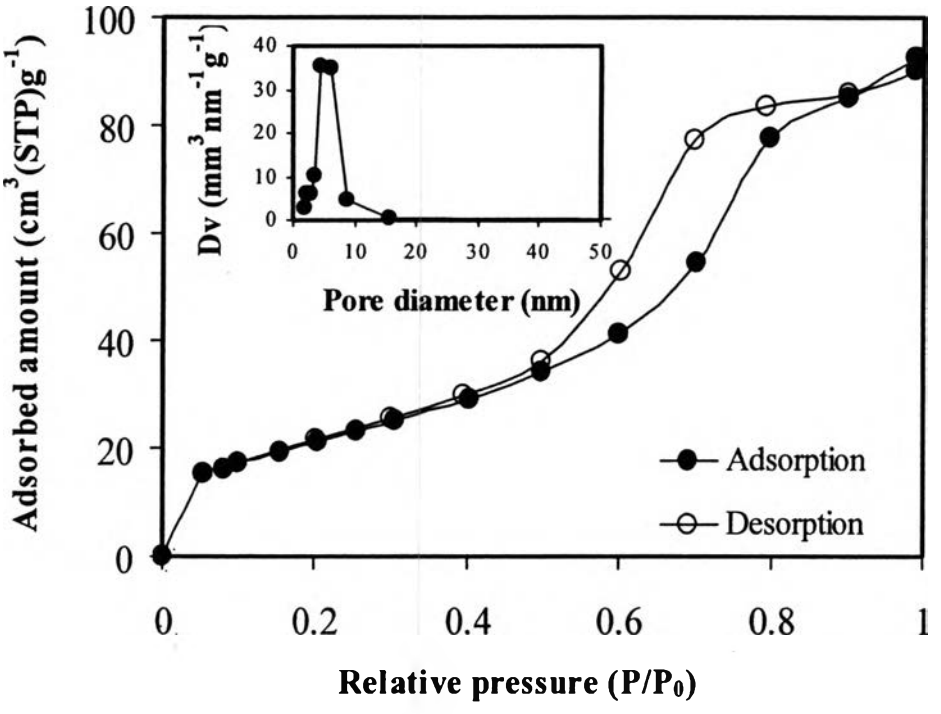

Figure 4.24 N_2 adsorption-desorption isotherms of the synthesized 0.6 wt.% Pt-loaded mesoporous-assembled TiO_2 calcined at 500°C for 4 h (Inset: Pore size distribution).

Table 4.6 Summary of textural properties obtained from N_2 adsorption-desorption results of the synthesized Pt-loaded mesoporous-assembled TiO_2 calcined at 500°C for 4 h with various Pt loading contents

Photocatalyst	Pt loading content (wt.%)	BET surface area (m^2g^{-1})	Mean pore diameter (nm)	Total pore volume (cm^3g^{-1})
Mesoporous-assembled TiO_2	0	84.3	6.18	0.158
	0.2	83.8	6.17	0.152
	0.4	85.6	6.15	0.162
	0.6	93.8	6.18	0.153
	0.8	91.1	6.17	0.152

The results from N_2 adsorption-desorption analysis show the change of surface area with respect to the different contents of Pt loading. It can be seen that the increase in surface area was observed when Pt was loaded on the mesoporous-assembled TiO_2. This might imply that the addition of Pt source during the sol-gel preparation step can help stabilize the mesopore due to inhibiting the coalescence of the TiO_2 nanoparticles for some extent during the calcination step. The highest surface area of 93.8 m^2g^{-1} was found when the 0.6 wt.% Pt was loaded on the investigated TiO_2 photocatalyst. However, the mean pore diameter and total pore volume of the Pt-loaded samples were insignificantly different from the unloaded one.

The XRD patterns of the synthesized Pt-loaded mesoporous-assembled TiO_2 photocatalyst with various Pt loading contents are shown in Figure 4.25. Table 4.7 also summarizes all results of XRD analysis, including crystalline phase and crystallite size.

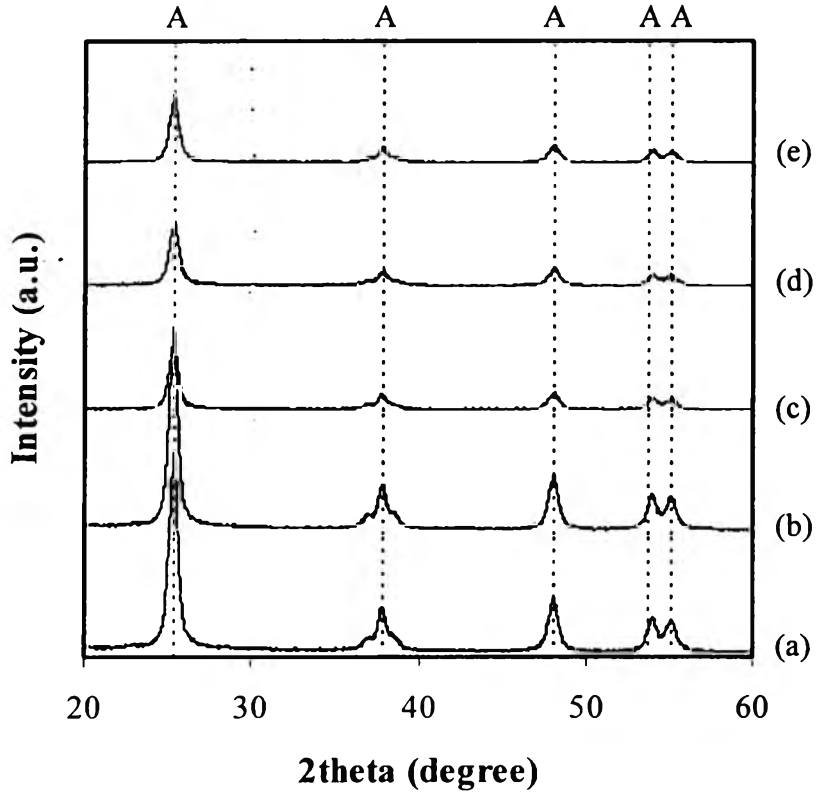

Figure 4.25 XRD patterns of synthesized Pt-loaded mesoporous-assembled TiO_2 calcined at 500°C with (a) 0 wt.% Pt, (b) 0.2 wt.% Pt, (c) 0.4 wt.% Pt, (d) 0.6 wt.% Pt, and (e) 0.8 wt.% Pt (A=Anatase).

The XRD diffractograms of the Pt-loaded samples are not quite different from that of the unloaded one, mainly showing the crystalline anatase phase. The indistinguishable presence of the diffraction peak of Pt at 39.8° indexed to (111) plane indicated that the loaded Pt particles were in a very high dispersion degree. As the minimum detection limit of the XRD technique is around 5 nm, it is inferred that the crystallite size of the Pt particles was approximately this value. From Table 4.7, the calculated anatase (101) crystallite size tended to insignificantly change with increasing Pt loading content, signifying similar degree of nanoparticle coalescence and growth. The results imply that the loaded Pt particles might not influence the TiO_2 crystallite formation due to similar TiO_2 crystallite size as compared with that without Pt loading, but might only influence the inhibition of TiO_2 particle coalescence due to the observed higher surface area.

Table 4.7 Summary of XRD analysis of the synthesized Pt-loaded mesoporous-assembled TiO_2 calcined at 500°C for 4 h with various Pt loading contents

Pt loading content (wt.%)	Phase from XRD pattern	Anatase (101) crystallite size (nm)
0.0	Anatase	13.64
0.2	Anatase	14.26
0.4	Anatase	14.89
0.6	Anatase	14.26
0.8	Anatase	13.70

The UV-Vis spectra of synthesized Pt-loaded mesoporous-assembled TiO_2 photocatalyst calcined at 500°C for 4 h with various Pt loading contents are shown in Figure 4.26. The results indicate that the absorption onsets of all Pt-loaded samples are not quite different from each other, as well as from the unloaded one shown in Figure 4.8, which appeared approximately at 387 nm, corresponding to the band gap energy of anatase TiO_2 of 3.2 eV.

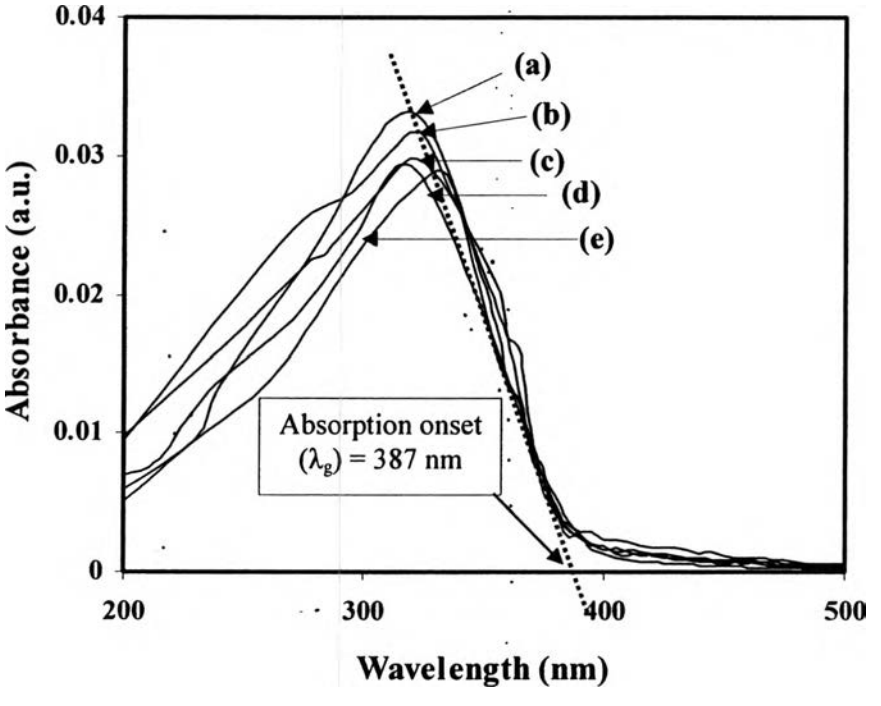

Figure 4.26 UV-Vis spectra of synthesized Pt-loaded mesoporous-assembled TiO_2 calcined at 500°C with (a) 0.2 wt.% Pt, (b) 0.4 wt.% Pt, (c) 0.6 wt.% Pt, and (d) 0.8 wt.% Pt.

From SEM-EDX analysis of the 0.6 wt.% Pt-loaded mesoporous-assembled TiO_2 as shown in Figure 4.27, the Pt content from elemental mapping of the sample was examined to be approximately 0.6 wt.%. From the EDX area mapping, it can be clearly seen that the Pt species well and uniformly dispersed throughout the Pt-loaded sample. From TEM-EDX analysis shown in Figure 4.28, dark patch in the TEM image indicates high electron density, and it corresponds to the deposition of Pt nanoparticle, as confirmed by the EDX point mapping. The particle size of Pt was observed to be approximately 5 nm, which certainly agrees with the XRD result.

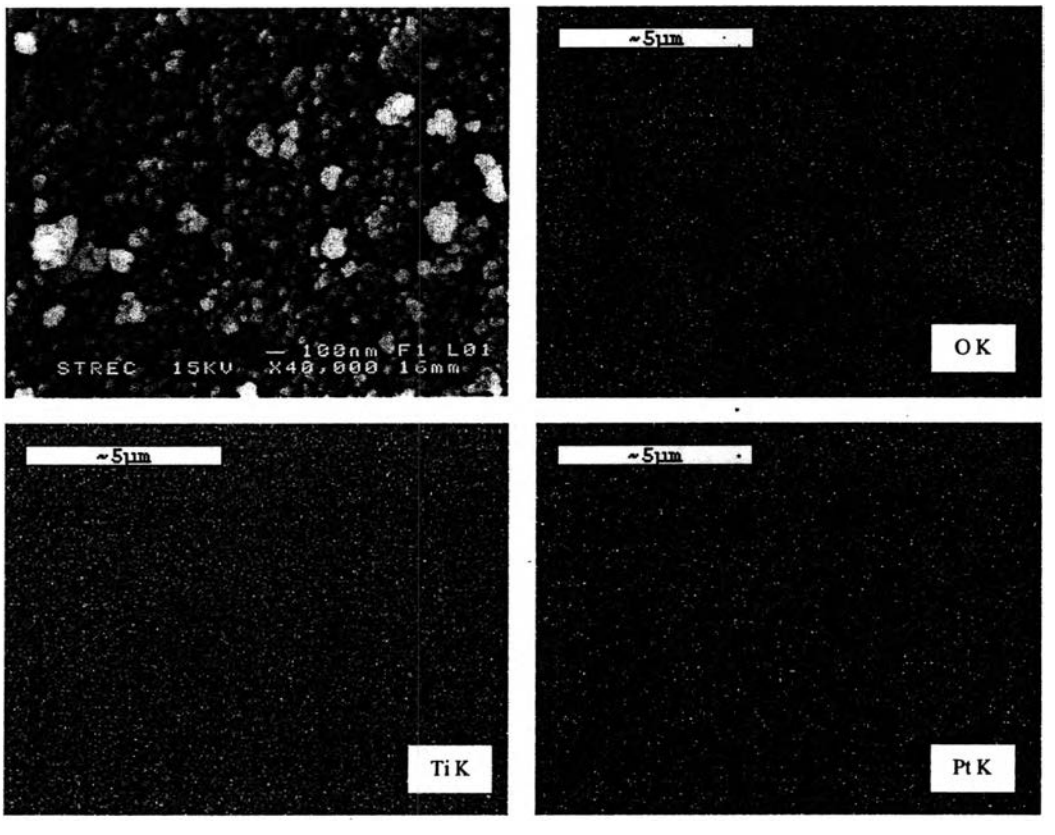

Figure 4.27 SEM image and EDX area mappings of synthesized 0.6 wt.% Pt-loaded mesoporous-assembled TiO_2 photocatalyst calcined at 500°C for 4 h.

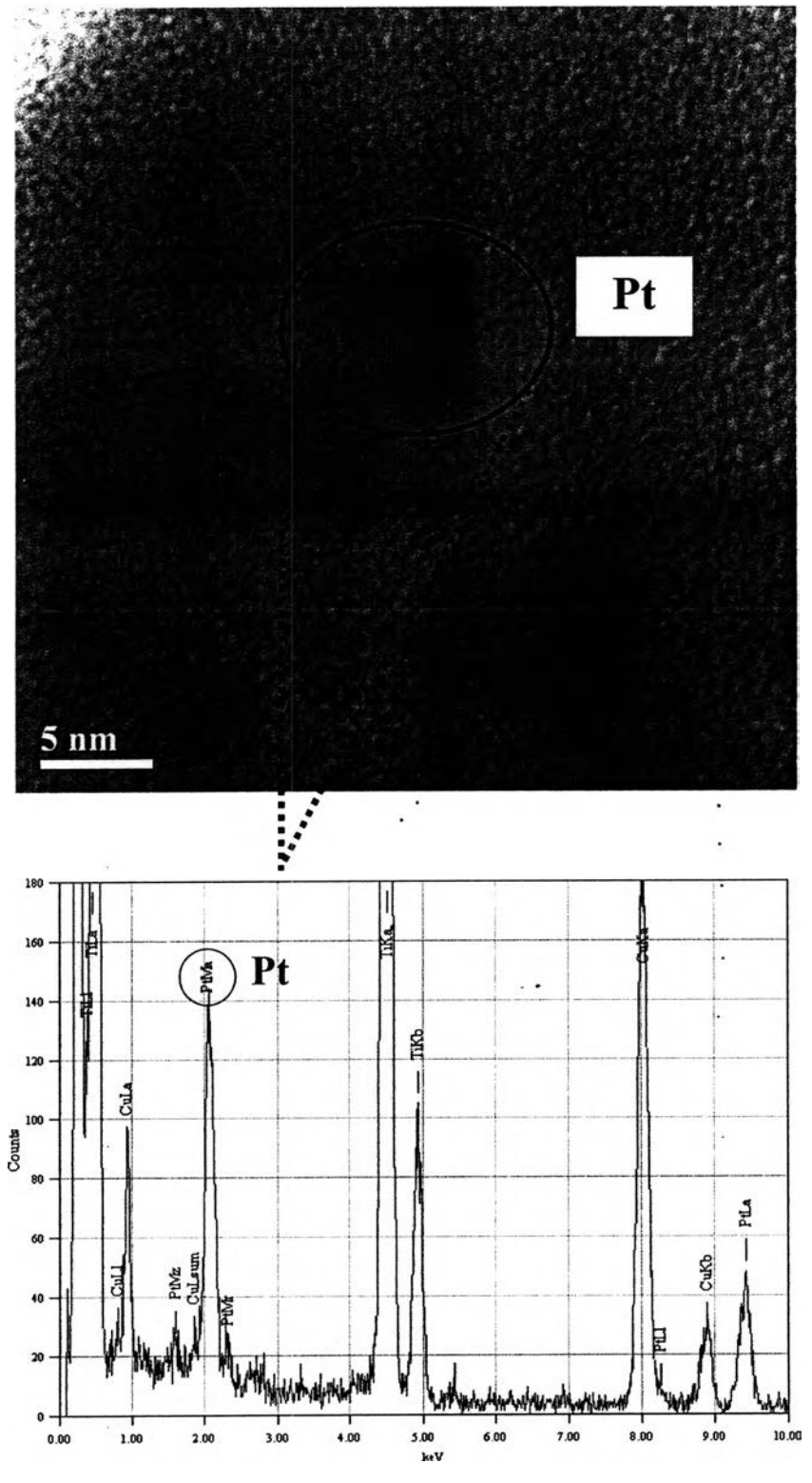

Figure 4.28 TEM image and EDX point mapping of synthesized 0.6 wt.% Pt-loaded mesoporous-assembled TiO_2 photocatalyst calcined at 500°C for 4 h.

The photocatalytic decolorization rate constant (k) of MO over the synthesized Pt-loaded mesoporous-assembled TiO_2 photocatalyst calcined at 500°C for 4 h with various Pt loading contents is shown in Figure 4.29. The optimum reaction conditions previously obtained were used for the photocatalytic MO decomposition study. Note that for the effect of Pt loading, the degradation of aromatic part of MO could not be examined as well due to the interference of the added H_2O_2 no the absorbance peak at 270 nm. Therefore, the decolorization of MO was only investigated.

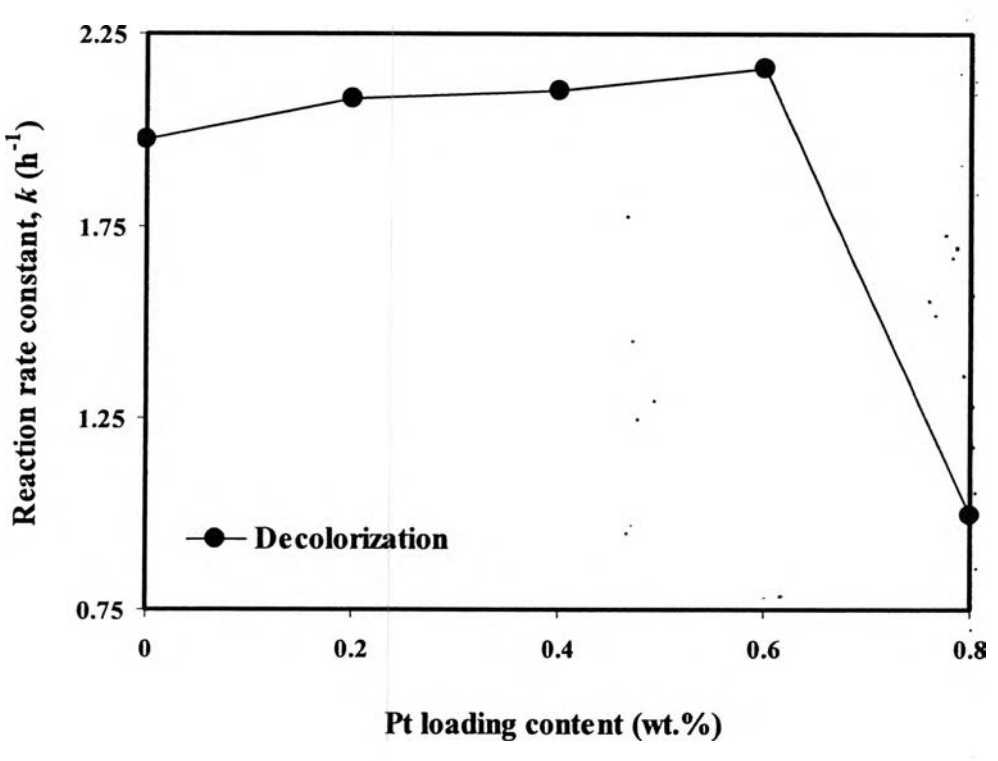

Figure 4.29 Effect of Pt loading content on reaction rate constant for decolorization of MO by synthesized Pt-loaded mesoporous-assembled TiO_2 photocatalyst calcined at 500°C for 4 h (initial MO concentration = 5 mg/l; photocatalyst dosage = 7 g/l; H_2O_2 concentration = 0.5 M; initial solution pH = 4.7; reaction volume = 80 ml; irradiation time = 4 h).

Figure 4.29 shows that the Pt loading content affected the photocatalytic decomposition of MO. From the experimental results, the increase in Pt loading content up to 0.6 wt.% could increase the photocatalytic activity because of the increase in the active sites. However, the photocatalytic activity dramatically diminished with further increasing Pt loading content. These reveal that the optimum Pt loading content exists for the investigated system at 0.6 wt.%, exhibiting the reaction rate constant of 2.16 h^{-1}. The photocatalytic activity results also well agree with the BET surface area results, showing the highest value at 0.6 wt.% Pt loading content. This can be explained in that with the initial increase in the Pt loading content, TiO_2 nanoparticles may carry more Pt nanoparticles, which are indispensable for the removal of the photogenerated electrons from TiO_2 conduction band for the formation of more aforementioned active radical species, leading to an increase in the photocatalytic activity. When increasing the Pt loading content beyond the optimum value, even though more Pt nanoparticles were deposited on the TiO_2 particles, the decrement in the photocatalytic activity might be attributed to the excess of Pt nanoparticles on the photosensitive TiO_2 surface, which caused the decrease in the light absorption capability and accordingly lowered the photoexcitation to generate the active electrons (Choi *et al.*, 1994). The increase in Pt loading content over 0.6 wt.% also showed the decrease in the reaction rate to a lower level than that of the unloaded TiO_2, plausibly because the excess Pt can behave as charge recombination center instead of charge separation center. In addition, it has to be noted that since the mesoporous-assembled TiO_2 photocatalyst without Pt loading already provided a considerably high photocatalytic decomposition efficiency under the optimum reaction conditions, the Pt loading at the optimum value insignificantly enhanced the efficiency, only for a small extent, as shown from the increase in the decolorization rate constant from 1.97 to 2.16 h^{-1}.